

CORE - A Cell-Level Coarse-to-Fine Image Registration Engine for Multi-stain Image Alignment

Esha Sadia Nasir¹, Behnaz Elhaminia¹, Mark Eastwood¹, Catherine King², Owen Cain⁴, Lorraine Harper^{3,5}, Paul Moss², Dimitrios Chanouzas^{2,3}, David Snead^{1,6}, Nasir Rajpoot^{1,6}, Adam Shephard¹, and Shan E Ahmed Raza¹

¹Tissue Image Analytics (TIA) Centre, Department of Computer Science, University of Warwick, UK.

²Department of Immunology and Immunotherapy, College of Medicine and Health, University of Birmingham, UK.

³Renal Unit, Queen Elizabeth Hospital Birmingham, University Hospitals Birmingham NHS Foundation Trust, UK.

⁴Department of Cellular Pathology, Queen Elizabeth Hospital Birmingham, UK.

⁵Department of Applied Health Sciences, College of Medicine and Health, University of Birmingham, UK

⁶Histofy Ltd, Coventry, UK.

Abstract

Accurate and efficient registration of whole slide images (WSIs) is essential for high-resolution, nuclei-level analysis in multi-stained tissue slides. We propose a novel coarse-to-fine framework **CORE** for accurate nuclei-level registration across diverse multimodal whole-slide image (WSI) datasets. The coarse registration stage leverages prompt-based tissue mask extraction to effectively filter out artefacts and non-tissue regions, followed by global alignment using tissue morphology and accelerated dense feature matching with a pre-trained feature extractor. From the coarsely aligned slides, nuclei centroids are detected and subjected to fine-grained rigid registration using a custom, shape-aware point-set registration model. Finally, non-rigid alignment at the cellular level is achieved by estimating a non-linear displacement field using Coherent Point Drift (CPD). Our approach benefits from automatically generated nuclei that enhance the accuracy of deformable registration and ensure precise nuclei-level correspondence across modalities. The proposed model is evaluated on three publicly available WSI registration datasets, and two private datasets. We show that **CORE** outperforms current state-of-the-art methods in terms of generalisability, precision, and robustness in bright-field and immunofluorescence microscopy WSIs.

Keywords: Registration, Microscopy, Multimodal, Nuclei, Alignment, Morphology, Deformation

1 Introduction

In computational pathology, extensive research has been directed towards biomarker discovery, characterisation of tissue architecture, and disease sub-typing through the analysis of multi-stained whole slide images (WSI). Since raw tissue samples are inherently transparent, they are typically stained with haematoxylin and eosin (H&E), immunohistochemistry (IHC), multiplex immunofluorescence (mIF), or periodic acid-schiff (PAS) after fixation on glass slides. These stained samples are then scanned to generate high-resolution digital WSIs, which are then used for downstream analyses, such as biomarker identification and investigation of disease progression. To achieve a comprehensive understanding of tissue morphology and pathology, it is often necessary to integrate information from multiple stains. This requires precise WSI registration to enable joint analysis across different staining modalities. Image registration refers to the process of determining a transformation that maps corresponding elements of a source image to a target image. This transformation maps both images originating from different coordinate systems into a common coordinate space, allowing for an accurate and meaningful comparison.

WSI registration is typically applied to **consecutive** or **re-stained** slides, depending on the tissue slicing criteria. Each protocol presents distinct challenges, primarily due to variations in tissue deformation and the availability of characteristic features necessary for accurate alignment [1]. Since re-stained slides represent the same tissue section, images can generally be aligned with higher accuracy after registration. In contrast, consecutive slides, while originating from the same tissue block, represent different physical sections. This makes it more challenging to identify the corresponding structures on the slides. The difficulty increases as the distance between sections grows, as the same tissue features may no longer be present in both slides [2]. Despite differences in the level of complexity, both re-stained and consecutive section slides present challenges due to non-linear tissue deformations and tissue loss that may occur due to the chemical reactions and mechanical handling involved in the removal and application of the stain.

Different stains and imaging modalities such as H&E, IHC, PAS and mIF highlight distinctive tissue components, leading to variations in contrast and texture. As a result, features that are prominent in one stain (or modality) may be faint or absent in another, making feature matching extremely challenging. Additionally, tissue sections often undergo both elastic deformations (such as stretching) and inelastic deformations (such as tear or missing regions) during preparation, further complicating alignment. Variability in section thickness and tissue handling can also change the appearance of the same tissue across slides, adding another layer of complexity. The digitisation process may introduce artefacts, such as blurriness, dust, and folds that degrade image quality and can mislead registration algorithms. Moreover, the high resolution of WSIs demands substantial computational power and storage, which poses practical challenges for efficient processing. Unlike conventional medical images such as MRI or CT scans, WSIs typically lack consistent landmarks across stains and modalities, making classic computer vision image registration techniques less effective. These challenges necessitate the need for specialised algorithms capable of robust and efficient registration, even in the presence of significant appearance and structural variability. Our work addresses these limitations by proposing a *stain-agnostic, nuclei-point based* registration framework that generalises across staining protocols without manual tuning. We formulate registration as a two-stage process: a coarse alignment based on prompt-guided tissue segmentation masks, followed by a fine-grained nuclei-level point set registration. This hybrid approach enables robust alignment

across stain combinations (e.g., H&E-mIF, H&E-IHC, H&E-PAS) while preserving tissue structure and achieving high accuracy.

The main contributions of our proposed work are as follows:

- **A multimodal WSI registration algorithm** - We introduce a multimodal WSI registration algorithm capable of aligning H&E-stained slides with PAS, mIHC, and mIF, including cross-modal combinations i.e., bright field and immunofluorescence microscopy images such as H&E-mIF.
- **A novel multi-scale WSI registration method** - A novel multi-scale WSI registration method that supports deformable registration at both coarse and fine (high resolution alignment at 20 \times) levels.
- **High computational efficiency** - Our algorithm achieves state-of-the-art computational efficiency when compared at the coarse-level WSI registration, outperforming existing methods in speed and scalability.
- **Multi-stain, multi-modal evaluation** - The method has been evaluated on five cohorts, with multiple stains and modalities for consecutive and re-stained sections.
- **High resolution visualisation** - We provide real-time, high-resolution visualisation of both rigid and non-rigid deformations across the full WSIs, facilitating intuitive assessment and validation. A working demo of CORE registration is available at TiaViz Demo¹. Details for using TiaViz have been provided in Appendix A
- **Open-source code for reproducibility** - We provide open-source code through GitHub² to support reproducibility and future research and development in multimodal WSI registration.

2 Related Works

During the past decade, WSIs registration has attracted significant research attention, leading to noteworthy contributions. Despite these advances, the unique characteristics of multi-stained WSIs, including their gigapixel resolution, tissue variability, non-linear deformations, and staining inconsistencies, continue to pose major challenges. These factors often limit the effectiveness of conventional medical image registration methods, particularly when alignment at the nuclei level is required. A detailed review of the WSI registration methods has been presented in Elhaminia et al. [1].

The most notable recent approaches for WSI Registration include HistokatFusion [2], VALIS [3], DeeperHistReg [4], and DFBR [5]. Among these methods, HistokatFusion [2] and VALIS [3] both rely on traditional iterative image registration methodology while DFBR and DeeperHistReg are based on DL based feature extractors.

Lotz et al. [6] proposed an iterative intensity based method for low resolution global registration followed by patch-level refinement for local deformation estimation. HistokatFusion employs a three-stage registration pipeline [7], where the first stage performs

¹https://tiademos.dcs.warwick.ac.uk/bokeh_app?demo=WSIReg

²https://github.com/eshasadia/WSI_mIF_Reg.git

automatic rotation-based affine registration, followed by Gauss–Newton parametric optimisation, concluding the final stage with non-rigid B-spline regularisation. This method combines coarse initial alignment with non-rigid, intensity-driven iterative registration, using normalised gradient fields (NGF) as the similarity metric and B-spline transformations to capture deformations. The method secured first place in the ANHIR competition [8] and was ranked among the top performers in the ACROBAT [9] benchmark. However, the code for the method is not publicly available.

Gatenbee et al. [3] created the virtual alignment of the pathology image series (VALIS) WSI registration library. VALIS aligns mIHC, H&E and mIF WSIs. The method employs multiple techniques in preprocessing, rigid registration and non-rigid registration to optimise performance and reduce registration error. A notable observation is the combined use of both deep learning architectures such as VGG and hand-crafted feature descriptors, such as BRISK [10]. Although this method provides a practical solution for scalable whole-slide image (WSI) registration, its substantial computational overhead limits its efficiency.

Beyond intensity-based matching, some registration methods leverage fine-grained image features. Sarkar et al. [11] proposed a line-based strategy for aligning adjacent tissue sections selecting boundary points around the tissue and using RANSAC [12] to sample point pairs for line fitting. Alignment is guided by the sum of gradient magnitudes near these lines, with parameters such as line, angle and distance informing translation and rotation estimates. A multi-resolution normalised correlation on gradient magnitude images then refines local alignment. Huang et al. [13] employed morphological descriptors, including area and eccentricity of segmented red blood cells, while Cooper et al. [14] incorporated broader feature sets including centroid, area, eccentricity, and axis orientation from segmented H&E and CD3 stained images.

In the recent past, most of the proposed methods have utilised learning-based techniques, particularly **deep learning methods**. For instance, Wodzinski et al. [4] combined deep feature extractor (SuperPoint) [15] and matcher (SuperGlue) [16] with an intensity-based non-rigid alignment stage. Their approach improved high-resolution registration performance and addressed GPU memory limitations with a pyramidal strategy. Awan et al. [17] proposed an autoencoder-based model to learn deep feature representations of input image pairs. These features extracted from the autoencoder were then used to identify the optimal transformation through gradient descent. In another work, Awan et al. [5] proposed DFBR, the method comprises three primary stages, initial processing, rigid alignment, and non-linear registration. In the processing phase, tissue masks were generated and used for initial transformation estimation, then rigid transform is calculated by multi-scale CNN features extraction and matching pairs by considering the feature points with a small feature distance. Following the application of the DFBR method, any minor offset was corrected by a phase correlation method, subsequently followed by an established non-linear registration technique proposed in Lotz et al. [7].

Notably, several works have explored registration through features derived from segmented tissues. For example, Ge et al. [15] developed a multi-stain registration method that employed an unsupervised structural feature-guided (SFG) CNN, which was robust to both low-resolution rough and high-resolution fine structural features of tissues. The non-rigid network was pre-trained with the synthetic Flying Chair dataset [18]. Then the supervised component of the SFG network was trained on landmarks. Mahapatra et al. [19] leveraged deep segmentation maps from a pre-trained U-Net to guide non-linear alignment.

These approaches highlight the trend towards integrating tissue morphology, nuclei features, and learning-based representations.

For high resolution WSI registration, nuclei point based registration has been proposed in the recent past. Jeyasangar et al. [20] proposed a nuclei-based WSI registration method that detects nuclei using Hover-Net, extracts tile point sets, and aligns them via a Gaussian Mixture Model with Locally Linear Embedding to preserve local structures. This approach outperforms existing methods on a subset of the HYRECO [21] dataset and generalises to other stains. However, the evaluation was limited to a single stain and high resolution only. Recently, Jiang et al. [22] proposed a framework to align WSI images from different staining modalities specifically H&E and mIF at the cellular level using nuclei points. The method treats cell segmentation outcomes as point sets and employs CPD for initial alignment, followed by refinement using Graph Matching (GM). The method has been evaluated on the ovarian cancer tissue microarrays (TMAs) dataset, the approach achieves high alignment accuracy, facilitating the integration of cell-level features across modalities. However, the open-source implementation is only applicable to pre-extracted visual fields and TMAs only, and the method cannot be applied to WSI registration.

Although several studies have been evaluated at the coarse or fine level to evaluate the WSI registration performance for specific stain combinations, such as H&E to IHC [5, 2] or H&E to DAPI [23, 24], no existing method systematically achieves or assesses both coarse and fine level (high resolution) registration across a diverse set of stains and modalities including H&E, PAS, IHC and mIF. Despite recent advances, WSI registration remains limited in its use of intrinsic tissue features such as cells, nuclei, or blood vessels as the basis for alignment. Many existing methods still rely on stain-specific cues, rigid assumptions, or computationally intensive processes. As these stain-specific cues vary across stains, these methods often struggle with heterogeneous tissue morphology, staining variability, or severe deformations.

In this study, we address these challenges by leveraging nuclei as fine-grained, intrinsic features for precise and robust image registration. We propose and evaluate both coarse and fine level WSI registration approaches on consecutive sections and re-stained slides across multiple stains and modalities in this manuscript. Our analysis covers multimodal WSIs, including H&E, PAS, mIHC, and mIF stained slides.

3 Methodology

We propose a two-stage framework for multimodal WSI registration, designed to progressively refine spatial alignment across multiple resolutions. The proposed approach comprises (i) a coarse registration and (ii) a fine shape-aware registration stage for high resolution WSI alignment.

The coarse registration stage is optimised for speed and robustness, providing a rapid global alignment across modalities. This is particularly useful in scenarios where precise nuclei-level alignment is not required and computational efficiency is the primary concern.

After the initial coarse level registration, the fine shape-aware registration stage performs precise, nuclei-level alignment. By focusing on nuclei-level correspondence, the method enhances the registration accuracy and enables detailed downstream analysis. Together, these stages form an effective coarse-to-fine pipeline that addresses key challenges in multimodal WSI registration, including tissue deformation, staining variability,

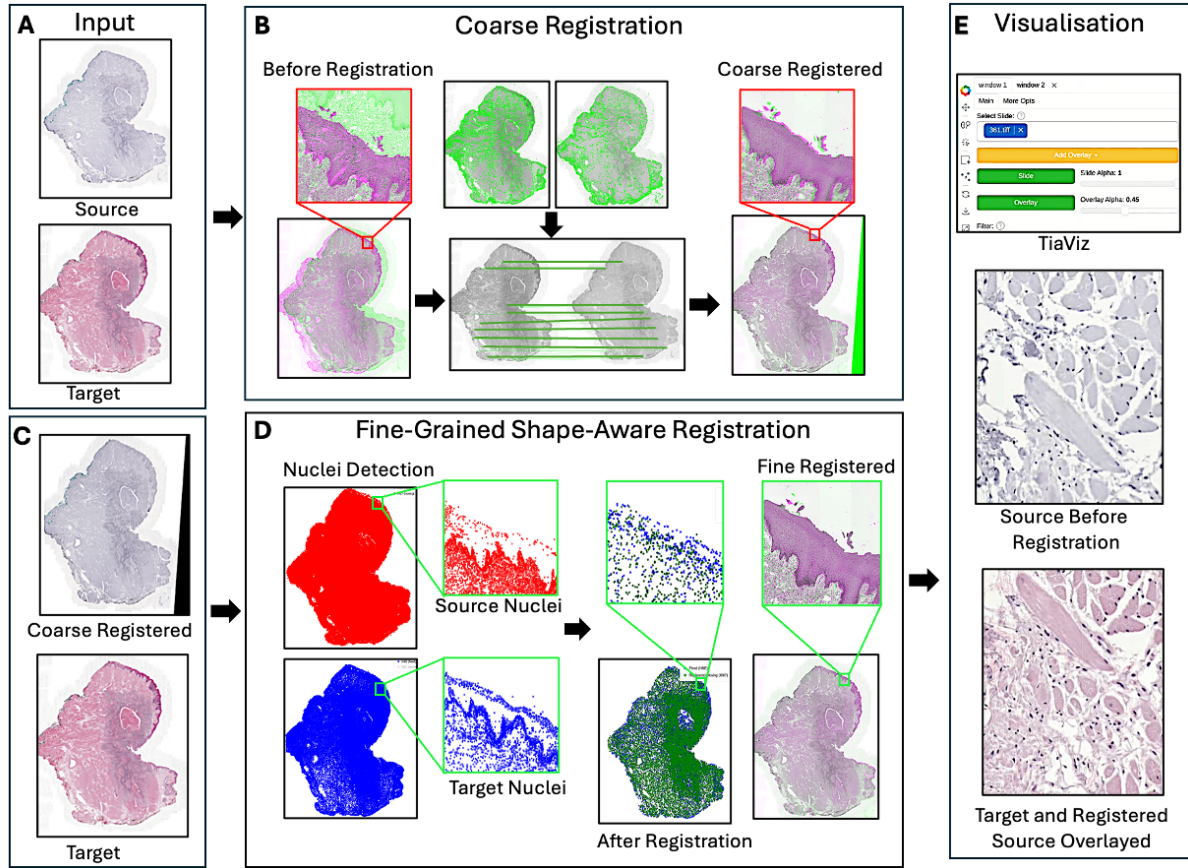


Figure 1: A high-level overview of the proposed WSI registration method (**CORE**). (A) Block shows input source and target slides. (B) The coarse registration block illustrates the overlay before transformation, the estimated (rigid+non-rigid) coarse alignment using feature matching, and the resulting coarse-registered overlay. (C) Shows the coarse registered source output and target slides. (D) Using the target and coarsely registered source, nuclei point sets are extracted, and fine shape-aware point set registration is performed to estimate local nuclei-level deformations. (E) The TIAViz visualisation tool enables real-time application of the registration to full-resolution slides.

and structural discrepancies. The proposed framework is designed with the goals of achieving both scalability and precision, aiming to provide a reliable foundation for high-throughput WSI analysis. A high level outline of the proposed approach is shown in Fig. 1.

3.1 Coarse Registration

The coarse registration step performs a low magnification WSI registration using initial preprocessing followed by rigid transformation and non-rigid deformation. A detailed stepwise coarse rigid registration block diagram is shown in Fig. 2. Individual steps have been discussed in the following sections.

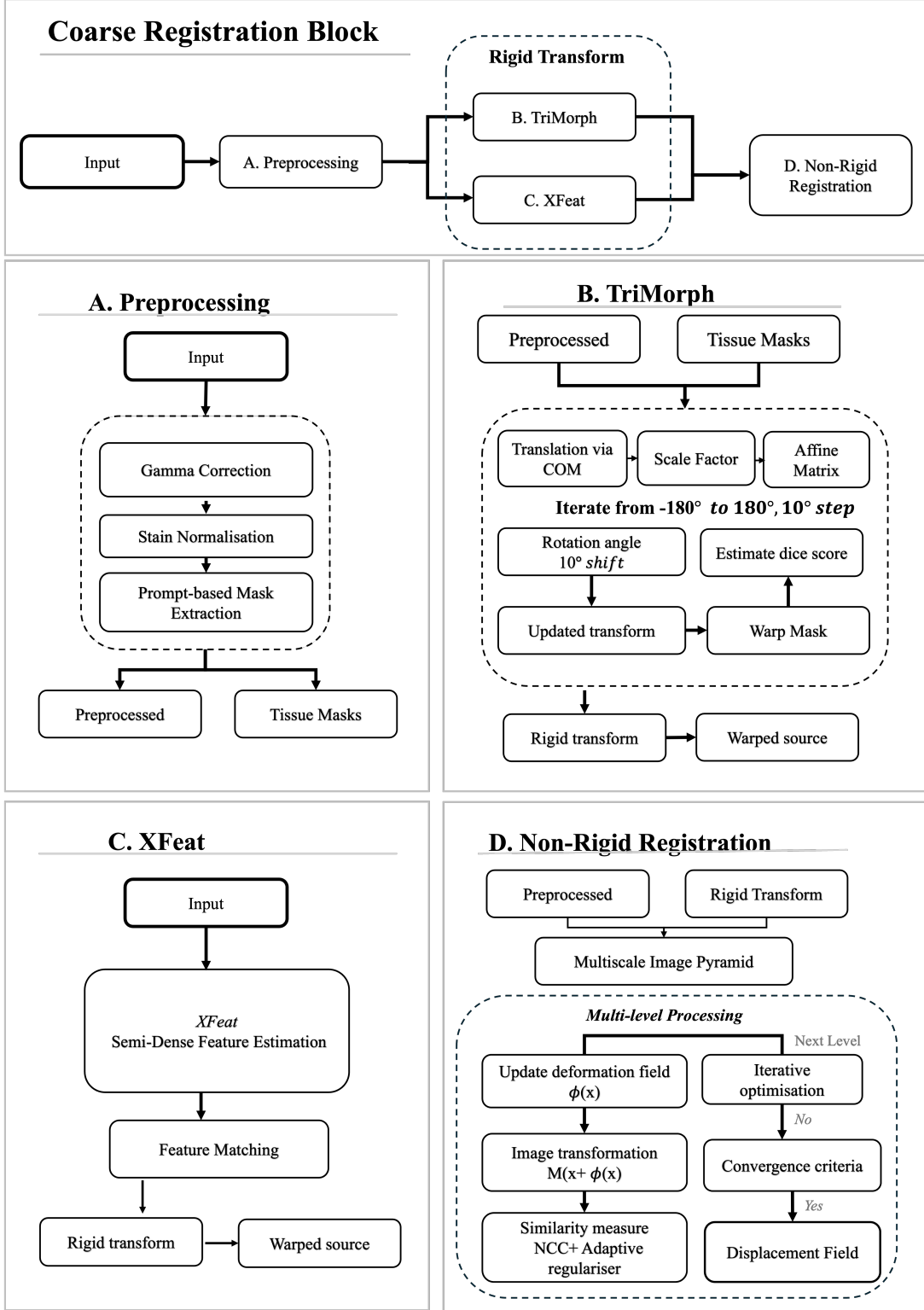


Figure 2: Coarse Rigid Registration Block. (A).The preprocessing and tissue mask extraction workflow applies gamma correction, stain normalisation, and prompt-based mask extraction. (B) The TriMorph block computes translation via COM (centre-of-mass) estimation, scale factor and rotation angle from input images and tissue masks. (C) XFeat block estimates semi-dense feature from inputs and perform rigid transform (D) Coarse Non-Rigid registration processing block based on iterative optimisation and adaptive regularisation based deformation estimation.

3.1.1 Preprocessing

The preprocessing pipeline begins by converting RGB images to greyscale, followed by gamma correction to enhance the visibility of poorly stained tissue features. For each WSI pair, downsampled thumbnails are extracted at $0.625\times$ and $1.25\times$ resolutions. Differential gamma correction is employed to enhance tissue contrast, with gamma values of $\gamma = 1.0\text{--}1.2$ for H&E-stained images and $\gamma = 0.4\text{--}0.8$ for IHC-stained images. These ranges were empirically determined based on evaluations conducted across the datasets.

Stain normalisation is then applied to improve tissue mask extraction for prompt-based segmentation.

Stain Normalisation To achieve consistent colour representation across WSIs, we apply Macenko stain normalisation [25], a well-established approach for standardising the appearance of H&E WSIs. We follow the original parameter settings proposed by Macenko ($I_o = 240$, $\alpha = 1$, $\beta = 0.15$) and apply the reference H&E stain vectors, \mathbf{H} : [0.650, 0.704, 0.286] and \mathbf{E} : [0.072, 0.990, 0.105] to ensure robust and consistent stain separation and normalisation. The preprocessing pipeline incorporates normalisation techniques to overcome inter-sample variability caused by inconsistent staining and imaging conditions. This approach is essential for producing standardised images, allowing the model to focus on relevant structural features without being influenced by colour discrepancies supporting accurate segmentation outcomes. However, the model does not rely solely on stain normalization. Tissue mask extraction can still perform effectively without stain normalisation, provided that the tissue remains clearly visible, a condition guaranteed by the preceding contrast enhancement stage. Further details are provided in Appendix A.

Prompt-based Tissue Mask Extraction Tissue segmentation forms critical foundation of our coarse registration framework. The approach incorporates a prompt-based approach leveraging Florence-2 [26], a multimodal vision foundation model, in conjunction with the Segment Anything Model (SAM) [27]. We use Florence2-SAM based instance segmentation with strategically selected prompts (tissue, stain, histology, cell, tissue). These prompts are applied in a cascaded manner beginning with the default (tissue, stain) prompt. This ensures robust detection of tissue regions while excluding artefacts such as pen marks. The method successfully detected accurate masks for most of the data. However, in some cases ($\sim 2\text{--}3\%$ of the WSIs in our dataset), due to poor tissue quality and staining, the method did not produce any tissue mask. For handling such cases, the algorithm automatically uses a pre-trained U-Net architecture trained on 179 tissue samples from the ACROBAT dataset [9] for segmenting tissue regions. The segmented tissue masks are subject to morphological operations (opening and closing) and connected component analysis to identify and preserve only the largest tissue regions. The resulting tissue masks allow the algorithm to focus exclusively on tissue regions, facilitating precise alignment even in challenging scenarios with significant deformations or staining inconsistencies.

3.1.2 Rigid Registration

The rigid registration phase establishes alignment between tissue sections using tissue morphology-based transformation estimation *TriMorph* followed by robust feature extraction and matching based on accelerated dense feature estimation with the help of *XFeat*. This preliminary transformation provides a reliable starting point for subsequent

fine-grained registration, effectively handling large-scale spatial discrepancies and global deformations.

Triple Morphology Transform (TriMorph) This module establishes initial spatial correspondence between WSI pairs through a robust coarse registration approach based on tissue morphology. This specialised component estimates three transformations i.e., translation, rotation, and scaling to effectively align tissue masks.

The tissue morphology is first aligned using a centre-of-mass (COM) alignment step, using the extracted binary tissue masks to compute the centroids of both the target and source images. Specifically, we calculate a transformation matrix \mathbf{W}_{com} that translates the centre of mass of the source image i.e., (x_s, y_s) , to align with that of the target image i.e., (x_t, y_t) . To address scale discrepancies between slides, the algorithm analyses the relative dimensions of tissue masks and computes the appropriate scale factors.

Following the scale adjustment, the system then explores rotational alignments by rotating one of the slides through a discrete set of angular increments (specifically, $\theta = 10^\circ$). For each candidate transformation, the algorithm quantitatively evaluates the degree of overlap between the tissue regions using the Dice coefficient. The transformation that yields the highest Dice coefficient is selected as the optimal coarse alignment, provided that it surpasses the empirically determined threshold of ($\text{Dice}_{\text{threshold}} = 0.7$). In cases, where optimal transformation is not achieved due to low threshold, the method returns identity transform.

Accelerated Dense Feature Extraction via XFeat The coarse registration feature extraction framework incorporates an accelerated feature-based alignment method utilising the XFeat model [28]. XFeat is a lightweight architecture for resource-efficient visual correspondence, well-suited to multimodal registration pipelines.

We use its sparse keypoint-based matching combined with semi-dense correspondence to extract dense features from each tissue, preserving fine structural details in whole-slide images (WSIs). This approach allows detection and matching of up to 16,000 distinctive keypoints between downsampled WSI pairs, effectively capturing complex structural patterns in multi-stained specimens. A precision threshold of 3–5 pixels and up to 1,000–2,000 iterations are applied at a 99.9% confidence level to robustly filter outliers while retaining true correspondences.

Finally, to determine the optimal transformation, we evaluate the quality of the rigid transformations obtained using TriMorph and XFeat. This evaluation is based on Normalised Gradient Fields (NGFs), which measure image alignment by comparing the gradient orientations of the warped source and target images. NGFs calculate normalised image gradients and assess their similarity through dot products, offering a robust metric for quantifying edge alignment and structural correspondence.

$$\text{NGF} = \frac{1}{N} \sum_{i=1}^N \left(\frac{\nabla I_t}{\sqrt{|\nabla I_t|^2 + \epsilon}} \cdot \frac{\nabla I_s}{\sqrt{|\nabla I_s|^2 + \epsilon}} \right)^2 \quad (1)$$

Equation 1 defines NGF as ∇I_t and ∇I_s are the gradients of the target and source images, and $\epsilon = 0.01$ prevents division by zero.

3.1.3 Non-Rigid Registration

To address complex non-rigid spatial deformations present in WSIs, we propose a hierarchical deformation-based registration framework. Our framework builds on established hierarchical strategies used in both classical approaches (e.g., ANTs [29]) and learning-based models (e.g., VoxelMorph [30], DeeperHistReg [4]), which estimate deformations in a multi-resolution manner to ensure stable convergence and improved capture of multi-scale variations.

We employ a multi-level image pyramid, where alignment begins at low resolutions to estimate large-scale displacements, and progressively refines these estimates at higher resolutions to capture fine-grained local variations.

The spatial correspondence between source and target images is modelled using a dense displacement field defined over a regular grid. At each resolution level of the pyramid, this displacement field is updated to minimise a cost function that balances structural similarity and deformation smoothness. Optimisation is performed using the Adam optimiser for its efficiency and resilience to varying parameter scales. The similarity component of the cost function is based on NCC, which is robust to local intensity differences frequently encountered across diverse histological stains.

To ensure smooth deformations, we incorporate a smoothness regulariser inspired by the formulation of Ruan et al. [31], which includes both homogeneous and spatially adaptive components. We employ only the homogeneous regularisation component, which penalises abrupt variations in the displacement field and promotes smooth global transformations. This is formalised as:

$$R(\mathbf{D}) = \gamma_s \|\nabla \mathbf{D}\|_{\text{Frob}}^2 \quad (2)$$

where in equation 2:

- \mathbf{D} denotes the displacement field,
- $\nabla \mathbf{D}$ is the spatial gradient of the displacement field,
- $\|\cdot\|_{\text{Frob}}$ represents the Frobenius norm, and
- γ_s is a scalar weight controlling the strength of the smoothness regularisation.

The registration algorithm is implemented using grid-based spatial transformations and bilinear interpolation. At each pyramid level, the displacement field is refined and propagated to the next higher resolution via upsampling to 6 levels in the pyramid up to $1.25\times$ resolution. The modular design of the framework allows precise control over resolution depth, optimiser parameters, and regularisation strength at each level. Our experiments across a diverse range of tissue sections and staining modalities confirm the robustness of the proposed approach. The method reliably aligns WSIs affected by physical deformation, staining variability, and scanning inconsistencies.

For deformation estimation, we employ local NCC as the primary similarity metric with window size of 7 for cost estimation during each iteration:

$$\text{NCC} = \frac{\sum_{i=1}^N (I_t(i) - \bar{I}_t)(I_s(i) - \bar{I}_s)}{\sqrt{\sum_{i=1}^N (I_t(i) - \bar{I}_t)^2 \sum_{i=1}^N (I_s(i) - \bar{I}_s)^2}} \quad (3)$$

where I_t and I_s represent the target and source images, \bar{I}_t and \bar{I}_s denote their respective mean intensities, and N indicates the number of pixels in the overlap region. Table A.2 presents all the parameters used for coarse-level deformation estimation along with their corresponding values.

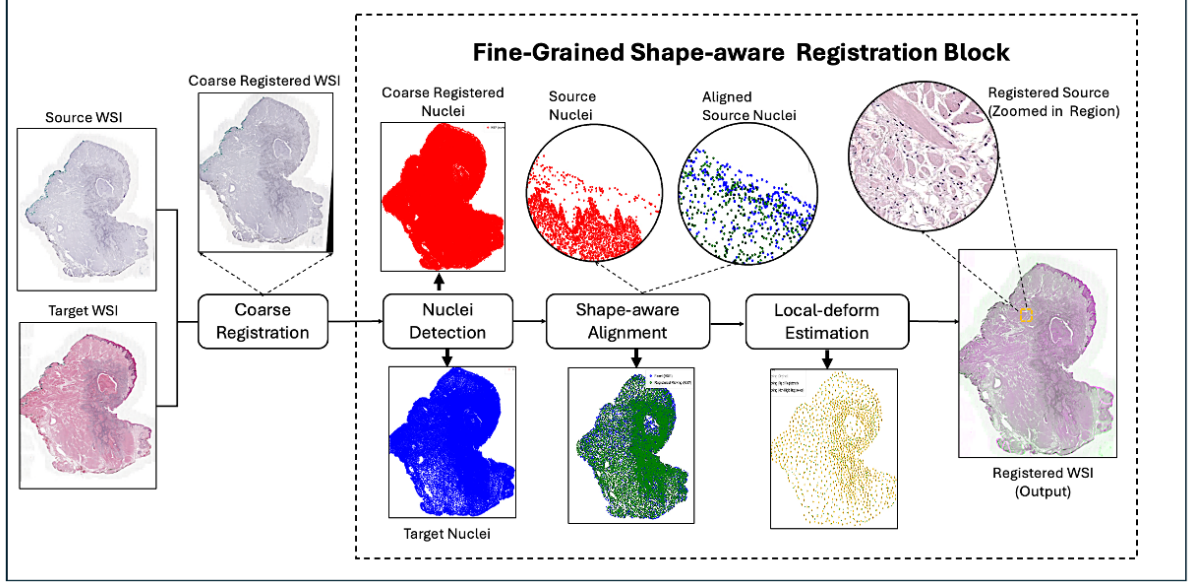


Figure 3: Proposed fine shape-aware nuclei point set registration. First coarse displacement field is applied on source WSI resulting in Coarse registered WSI. Nuclei point set are detected from Target and Coarse Registered WSI and then shape aware alignment using nuclei points is performed followed by local deform estimation.

3.2 Fine-Grained Shape-Aware Registration

For local-level deformation estimation, we propose a fine-grained, shape-aware registration framework designed to address tissue-level deformations by aligning nuclei centroids extracted from WSIs at $20\times$ or $40\times$. The method aims to enable precise correspondence at the nuclear level between source and target nuclei point sets, for both consecutive and re-stained tissue sections. Fig. 3 shows fine-grained shape-aware pointset registration block for nuclei level WSI registration.

By focusing on fine-scale point-set registration, the framework aims to ensure reliable spatial alignment of nuclei across different staining conditions and imaging modalities, while preserving key morphological characteristics. The core of our fine-grained shape registration module is based on nuclei point set detection followed by shape-aware transformation estimation.

Nuclei Point-set Detection To detect nuclei point sets, we tested both classic computer vision techniques and advanced DL models for registration. For the purpose of WSI alignment, we found sparse nuclei matching to produce equivalent results to a dense nuclei matching. Furthermore, matching dense set of nuclei has been shown to be computationally more expensive compared to sparse nuclei matching [20]. Therefore, for

computational efficiency, we employ a morphology-based nuclei detection pipeline optimised for whole-slide image (WSI) analysis. For this purpose, each WSI is first divided into non-overlapping patches of size 1000×1000 pixels at the highest resolution level. Patches are converted to greyscale, and an adaptive threshold is applied to binarise the image based on local intensity statistics.

Next, **H-maxima** and **H-minima** (morphological operations used to filter local maxima and minima) transforms are used to detect local intensity extrema corresponding to nuclear regions. These extrema serve as seed points for a marker-controlled watershed segmentation. The watershed algorithm operates on the distance transform of the binary mask, using the detected minima as markers, enabling effective separation of clustered or overlapping nuclei while preserving precise boundary definitions.

Following segmentation, nuclei centroids are computed and mapped from patch-level coordinates to global WSI coordinates, ensuring spatial consistency for downstream analysis and registration tasks.

The fine-grained shape-aware registration takes coarsely registered source nuclei and target nuclei centroids as an input and comprises two main stages:

- **Shape-aware Alignment:** This step further refines coarsely aligned WSI pairs for global transformations, including translation, rotation, and scaling using nuclei points.
- **Local-deform Estimation:** A subsequent step that compensates for local deformations, enabling precise alignment of nuclei distributions across sections.

3.2.1 Shape-aware Alignment

Given two point sets (source and target) representing nuclei coordinates from different imaging modalities, we define the local shape aware alignment problem as finding the optimal transformation \mathbf{W} that minimises the combined spatial and morphological distance between corresponding points. Let $\mathbf{S} = \{\mathbf{s}_1, \mathbf{s}_2, \dots, \mathbf{s}_n\}$ be the source point set and $\mathbf{T} = \{\mathbf{t}_1, \mathbf{t}_2, \dots, \mathbf{t}_m\}$ the target point set, where each point $\mathbf{p}_i = (x_i, y_i)$ includes spatial coordinates.

The transformation is parameterised by $\theta = [w_x, w_y, \phi, sc]$ for translation, rotation, and scaling as given in equation 4:

$$\mathbf{W}(x, y) = sc \begin{bmatrix} \cos \phi & -\sin \phi \\ \sin \phi & \cos \phi \end{bmatrix} \begin{bmatrix} x \\ y \end{bmatrix} + \begin{bmatrix} w_x \\ w_y \end{bmatrix} \quad (4)$$

Shape-aware distance metric We introduce a hybrid distance metric combining spatial proximity and morphological similarity in equation 5:

$$d(\mathbf{s}_i, \mathbf{t}_j) = (1 - \gamma) \cdot \|\mathbf{W}(\mathbf{s}_i) - \mathbf{t}_j\|_2 + \gamma \cdot |\hat{d}_i - \hat{d}_j| \quad (5)$$

where $\gamma \in [0, 1]$ is the shape weight parameter, \mathbf{W} is the transformation, and \hat{d}_i, \hat{d}_j are normalised shape attributes estimated from shape area i.e per nuclei area corresponding to the coordinates.

Shape Attribute normalisation

$$\hat{d}_i = \frac{d_i - d_{\min}}{d_{\max} - d_{\min}} \quad (6)$$

with d_{\min} and d_{\max} being global min/max shape values across both point sets in equation 6.

Objective Function

$$E(\theta) = \frac{1}{N} \sum_{i=1}^N \min_j \text{dist}(\mathbf{W}(\mathbf{s}_i; \theta), \mathbf{t}_j) \quad (7)$$

where N is the number of source nuclei centroids \mathbf{s}_i . We use k - d tree queries followed by shape-aware refinement. For each transformed point $\mathbf{W}(\mathbf{s}_i)$, we find the corresponding \mathbf{t}_j minimising the hybrid distance.

We use Powell’s derivative-free optimisation and iteration continues until:

$$\|\theta^{i+1} - \theta^i\|_2 < \varepsilon \quad \text{or} \quad i > i_{\max} \quad (8)$$

where $\varepsilon = 1 \times 10^{-8}$ is the small convergence threshold, and i_{\max} is the maximum iteration count in Equation 8. Table A.3 lists all the parameters used for shape-aware alignment along with its range and default values.

Shape Weight (γ): In our evaluation, we set the shape weight γ to 0.3, which provides a balanced contribution from morphological features. The impact of different γ values is summarised below:

- $\gamma < 0.1$: Morphological features are largely ignored.
- $\gamma \in [0.2, 0.4]$: Achieves an optimal balance between morphology and extreme transformation.
- $\gamma > 0.5$: Model tends to overfit to shape information.

Convergence Behaviour: To determine the optimal convergence point, the algorithm is executed for approximately ~ 150 iterations, which is generally sufficient to achieve the optimal transformation. A smaller value of ε enhances accuracy but increases computational cost.

When working with re-stained slides, we performed shape-aware alignment using the complete set of detected nuclei points at the highest resolution. This approach is effective because the underlying tissue architecture remains physically identical across staining iterations, allowing for direct nuclei-to-nuclei correspondence matching with minimal spatial variation.

To obtain an optimal solution for consecutive sections in minimal time, we implemented progressive sample size scaling for alignment optimisation. The process begins with an initial subsample of 500 nuclei centroids and iteratively doubles the sample size up to a maximum of $\sim 200,000$ points, enabling a comprehensive evaluation of registration performance across varying data densities. From the iterative transformations the transformation with minimum final error is selected. This adaptation is necessary as consecutive sections, despite their proximity, exhibit natural biological variations in both

nuclei positioning and overall tissue morphology. The algorithm prioritises preserving macroscopic tissue architecture while accommodating microscopic structural differences.

This progressive sampling strategy provides insight into the trade-off between computational efficiency and registration performance. Our results indicate that registration accuracy stabilises at intermediate sample size nearly $\sim 150,000$ points.

3.2.2 Local Deformation Estimation

After shape-aware alignment, local deformations are refined using the CPD algorithm [32], which performs non-rigid registration between shape-aware registered point sets.

To provide CPD with reliable initial correspondences, we employ a mutual nearest neighbours (MNN) approach that enforces bidirectional consistency. This removes ambiguous matches and enhances the robustness of the registration. MNNs are computed by identifying pairs of points that are closest to each other between the two sets. Specifically, the algorithm first finds the nearest point in the source set for each target point, and then the nearest point in the target set for each source point. A pair is considered a mutual nearest neighbour if each point is the closest to the other. Table A.4 reports all the parameters used for non-rigid registration along with range and default values.

Given the source point-set $\mathbf{S} = \{\mathbf{s}_1, \dots, \mathbf{s}_n\}$ and the target set be $\mathbf{T} = \{\mathbf{t}_1, \dots, \mathbf{t}_m\}$. CPD models the registration as a probabilistic alignment problem, estimating a transformation that maps \mathbf{S} onto \mathbf{T} while accounting for noise and outliers.

Following registration, a dense displacement field is constructed by interpolating the displacements between corresponding source and transformed points over a regular grid, using linear or cubic interpolation. The resulting field is smoothed with a Gaussian filter and normalised with a blurred tissue mask to suppress edge artefacts. To maintain physical plausibility, the field is constrained by a maximum displacement threshold and validated using the Jacobian determinant. Regions indicating local folding (i.e., non-positive Jacobian determinant) are corrected by zeroing the displacement, ensuring a stable and anatomically realistic deformation field.

For our nuclei datasets with $|\mathcal{C}| \approx 5000$ MNN correspondences, the CPD algorithm converges efficiently while providing high-quality deformation estimates. Increasing the number of MNNs beyond 5000 leads to an exponential growth in CPD computation time, making the deformation unattainable in under an hour for a single slide pair, while yielding only minimal performance gains.

4 Experiments & Results

In this section, we discuss the datasets used in this study, followed by a comparison of the results obtained from the proposed model to state-of-the-art methods.

4.1 Datasets

We evaluated our proposed approach on three publicly available largest WSI registration datasets i.e., ACROBAT [9], ANHIR [8] and HYRECO [21] and two private datasets i.e., Multi-IHC CRC[5] and REACTIVAS [citation].

4.1.1 ACROBAT-AutomatiC Registration Of Breast cAncer Tissue

The ACROBAT [9] dataset comprises consecutive female breast cancer slides, including 750 training cases, 100 validation cases, and 303 test cases. These slides are stained using H&E, ER (Estrogen Receptor), Ki67 (Kiel 67), PGR (Progesterone Receptor), and HER2 (Human Epidermal Growth Factor Receptor 2), resulting in a total of 3,406 WSIs across the training, validation, and test sets.

4.1.2 ANHIR - Automatic Non-rigid Histological Image Registration

The ANHIR [8] dataset comprises a total of 481 image pairs, divided into 230 training pairs and 251 evaluation pairs. It features 8 distinct tissue types stained with 18 different stains, presenting significant challenges for analysis and registration tasks.

4.1.3 HYRECO- Hybrid Re-stained and Consecutive Histological Serial Sections

The HYRECO dataset comprises two complementary subsets. *Subset A* (consecutive section slides) contains 9 groups of consecutive tissue sections stained with H&E, CD8 (Cluster of Differentiation 8), CD45 (Cluster of Differentiation 45), and Ki67. PHH3 (Phosphohistone H3) stained slides were generated by bleaching and re-staining the original H&E sections using a t-CyCIF (tissue-based Cyclic Immunofluorescence) like technique. Each section includes 11–19 manually verified landmarks, resulting in 138 landmarks per stain and 690 in total. *Subset B* (re-stained slides) consists of 54 paired H&E–PHH3 images, containing a total of 2,303 annotated landmarks (approximately 43 per pair).

4.1.4 Multi-IHC CRC

The Multi-IHC CRC dataset, obtained from the University Hospitals Coventry and Warwickshire (UHCW) NHS Trust, comprising WSIs from 86 distinct patients [5]. Each case features 16 high-resolution slides scanned at $0.275\ \mu\text{m}/\text{px}$ with various stains including CK8/18 (Cytokeratin 8 and Cytokeratin 18), mismatch repair (MMR) markers (MLH1, MSH2, MSH6, PMS2), and H&E. For evaluation of registration methods, we selected 7 cases with 6 slides per case for direct comparison with Awan et al. 2023 [5]. A notable challenge is the significant structural variability between H&E and IHC slides (separated by approximately $50\ \mu\text{m}$), while consecutive IHC sections maintain higher structural correlation.

4.1.5 REACTIVAS

The REACTIVAS dataset [33] was acquired from the University Hospitals Birmingham NHS Foundation Trust. It consists of Renal biopsy samples stained using a variety of protocols, including H&E, PAS, and advanced mIF techniques. We have included 11 paired samples for all 3 staining protocols. The mIF modality offers rich cellular and molecular detail, enabling the simultaneous visualisation of multiple biomarkers within the same tissue section. This complements the structural information provided by traditional histological stains, enhancing the dataset’s value for integrative pathology research.

Table 1: Summary of datasets used in this study.

Dataset	Tissue / Stain Types	No. of Cases / Pairs	Resolution ($\mu\text{m}/\text{pixel}$)
ANHIR [8]	8 tissue types, 18 stains	230 train pairs, 251 eval pairs	0.17–2.29
ACROBAT [9]	Breast cancer, H&E, ER, KI67, PGR, HER2	750 train, 100 val, 303 test (4212 WSIs)	0.23
HYRECO [2]	Human tongue with small oral tumour, H&E, PHH3, CD8, CD45	9 consecutive, 54 re-stained pairs	0.24
Multi-IHC CRC [5]	Colorectal, H&E, CK8/18, MMR markers	7 eval cases (105 reg. pairs)	0.275
REACTIVAS	Renal biopsies, H&E, PAS, mIF	11 paired samples	0.28

4.2 Evaluation Metrics

To quantitatively assess the accuracy of our registration framework, we employed two widely used metrics: Target Registration Error (TRE) and relative Target Registration Error (rTRE).

4.2.1 Target Registration Error (TRE)

The TRE quantifies the euclidean distance between corresponding landmark points in the target and registered source images. It is defined as:

$$\text{TRE} = \|P_t - T(P_s)\|_2 \quad (9)$$

where P_t denotes a landmark point in the target image, P_s is the corresponding point in the source image, and $T(\cdot)$ represents the transformation applied to align the source image with the target image. This metric captures the absolute spatial error after registration.

4.2.2 Relative Target Registration Error (rTRE)

To account for varying image sizes across datasets, we compute the relative TRE, which normalises TRE by a reference distance.

$$\text{rTRE} = \frac{\text{TRE}}{d_{\text{ref}}} \quad (10)$$

The reference distance in equation 10 d_{ref} is typically set to the diagonal length of the image. This normalisation ensures comparability of registration performance across datasets with different resolutions and dimensions.

The rTRE is particularly useful in multiresolution benchmarks such as ANHIR [8], where images vary in scale. Using rTRE, we ensure consistent and interpretable evaluation metrics in all test scenarios. Table A.1 presents the abbreviations and definitions of all metrics used in the evaluation. The choice of metric used in our analysis is based on the metric used in the original papers for the respective datasets for a fair comparison.

4.3 Results

We conducted computational experiments on NVIDIA Tesla V100-SXM3-32GB GPUs, which feature 32GB of high-bandwidth HBM2 memory and 640 Tensor Cores, enabling efficient execution of computationally intensive WSI registration algorithms. Although most of the existing methods are for coarse resolution, we have designed the method for both coarse and fine registration and report the results at both levels for fair comparison with the state-of-the-art existing approaches. Fine-shape aware registration was not conducted on the ACROBAT dataset, as the slides are available at $10\times$ resolution.

Table 2 presents a direct comparison between the proposed CORE method and current state-of-the-art approaches on the ACROBAT dataset [9], demonstrating superior performance and reduced computational time. The proposed method attains higher accuracy, as indicated by the AMTRE (90th percentile) metric, while requiring significantly less processing time than competing techniques. Fig. 4 illustrates representative target (H&E), source (IHC) and registered source slides from the ACROBAT dataset, together with the registration results overlay before and after alignment, and the corresponding extracted patch at full-resolution.

Table 3 presents a comparison between the proposed CORE method and existing state-of-the-art models on the ANHIR dataset [8], evaluated at both the coarse and fine registration stages. The results demonstrate improved performance and reduced runtime at coarse level. Fine-shape aware registration was performed only on slides available at $20\times$ and $40\times$ magnifications, while lower-resolution samples ($1.25\times$, $2.5\times$, $5\times$, and $10\times$) were excluded from fine resolution registration. Table A.6 reports step-wise results on the ANHIR dataset, summarising performance before initial alignment, after coarse alignment, and following fine alignment. Fig. 5 illustrates representative target (H&E), source (ER) and registered slides from the ANHIR dataset, along with the registration results overlay before and after alignment, and the corresponding extracted patch at full-resolution.

Table 4 presents comparative results of state-of-the-art models and the proposed CORE method on the HYRECO dataset, encompassing both re-stained and consecutive sections. In terms of the final median TRE for registration, the proposed method outperforms existing state-of-the-art approaches. We have also presented coarse and fine level rigid registration results of CORE and comparison with state-of-the-art approaches in Table A.5. It achieves substantially lower runtime across all comparisons at coarse level, providing a faster and more reliable registration. Table A.7 summarises step-wise results on the HYRECO dataset, detailing performance before initial alignment, after coarse alignment, and following fine alignment. Fig. 6 illustrates representative target (H&E), source (PHH3) and registered slides from the HYRECO dataset, along with the registration results overlay before and after alignment, and the corresponding extracted patch at full-resolution.

Following evaluation on public datasets, the proposed CORE method was further tested on private datasets. Table 5 presents a comparison between CORE and publicly available state-of-the-art models on the Multi-IHC CRC dataset, demonstrating superior performance at both coarse and fine registration stages, as indicated by lower TRE and reduced runtime. Table A.8 summarises step-wise results on the Multi-IHC CRC dataset, detailing performance before initial alignment, after coarse alignment, and following fine alignment. Fig. 7 illustrates representative target (CK818), source (MLH1) and registered slides from the Multi-IHC CRC dataset, along with the registration results overlay before and after alignment, and the corresponding extracted patch at full-resolution.

Table 6 presents the performance of the proposed CORE method on the REACTIVAS dataset, evaluated across H&E, PAS, and mIF modalities. The results demonstrate that our method achieves competitive performance compared with existing publicly available state-of-the-art approaches on PAS and mIF sections, attaining higher accuracy with reduced computational time at the coarse registration stage and improved precision at the fine, nuclei-level alignment stage. Table A.9 provides step-wise results for the REACTIVAS dataset, detailing performance before initial alignment, after coarse alignment, and following fine alignment. Fig. 8 illustrates these results before and after registration. Fig. 9 presents PAS and mIF registration on the REACTIVAS dataset, with panels from left to right showing the target (mIF), the source (PAS), and the registered overlay.

The results of our multimodal registration pipeline highlight several important insights regarding the challenges and opportunities in aligning WSIs stained with different modalities, including H&E, IHC, PAS, and mIF. Our coarse-to-fine approach successfully balances computational efficiency with high registration accuracy by combining global context through deep features and local precision via nuclei-based point set alignment.

Table 2: Performance comparison of **CORE** coarse method on **ACRO-BAT** Dataset: Median Performance Metrics (Lower Values Indicate Better Performance) in μm .

Resolution	Method	AMTRE-Per-centile90 [μm]	Mean Time (s)
Coarse	Initial	8556.00	-
	DFBR [5]	1447.36	50
	MEDAL	248.54	-
	NEMESIS	209.76	120
	Gestalt	149.08	-
	HistokatFusion [2]	141.64	50.1357
	DeeperHistReg [4]	140.33	70
	CORE	139.00	14.37

4.4 Discussion

In this work, we introduced CORE, a generalist framework for coarse-to-fine multimodal image registration. The CORE model incorporates two key innovations: a fast coarse registration stage, achieving alignment in approximately 15–20 seconds, and a fine-grained shape-aware nuclei-based registration designed to deliver precise cell-level alignment. For the design of CORE, we used Florence-SAM to generate tissue masks. We investigated the influence of image resolution on both coarse rigid transformation and deformation field estimation for consecutive and re-stained slides. Our analysis indicates that the best coarse-level registration performance is achieved at $0.625\times$ and $1.25\times$ objective resolutions. A key finding is that deep learning features, such as those extracted by XFeat, offer a robust way to capture modality invariant structural cues. These features enabled for effective coarse alignment despite significant differences in appearance and contrast between stains. This supports the growing evidence that deep learning methods are more

Table 3: Performance comparison of **CORE** coarse and fine methods with existing registration methods on the **ANHIR** dataset using relative Target Registration Error (rTRE). Results are presented with two aggregation levels: **Average** and **Median** across all image pairs. Methods are sorted by Average rTRE (AArTRE). The proposed *fine* method achieves the lowest error in both AArTRE and AMrTRE metrics.

Resolution	Method	Average rTRE		Median rTRE		Max rTRE		Mean Time (s)
		AArTRE [μm]	AMrTRE [μm]	MArTRE [μm]	MMrTRE [μm]	AMxrTRE [μm]	AMrTRE [μm]	
Coarse	Initial	0.1340	0.0684	0.1354	0.0665	0.2338	0.1157	-
	DFBR [5]	0.0055	0.0029	0.0040	0.0018	0.0275	0.0203	240
	AGH [34]	0.0053	0.0032	0.0036	0.0019	0.0283	0.0225	393
	DeeperHistReg [4]	0.0044	0.0029	0.0029	0.0017	0.0280	0.0225	120.00
	HistokatFusion [2]	0.0044	0.0027	0.0029	0.0018	0.0251	0.0188	9.6
	CKVST	0.0043	0.0032	0.0027	0.0023	0.0239	0.0189	468
	UPENN	0.0042	0.0029	0.0029	0.0019	0.0239	0.0190	960
	CORE	0.0040	0.00278	0.0026	0.0015	0.0240	0.0187	12
Fine	CORE	0.0034	0.0021	0.00245	0.0012	0.0323	0.018	1680

Table 4: Performance comparison of **CORE** method on the **HYRECO** Dataset (Consecutive and Re-stained Histological Sections) in μm . The proposed *fine* method achieves high precision in comparison with state-of-the-art for both Consecutive and Re-stained tissue types.

Resolution	Technique	Consecutive Sections			Re-stained Sections	
		AMTRE [μm]	AATRE [μm]	Avg Time (s)	AMTRE [μm]	Avg Time (s)
Fine	HistokatFusion [2]	5.30	-	1831	0.90	1831
	DeeperHistReg [35]	4.96	-	-	0.59	-
	CORE	4.35	-	2850	0.41	2850

Table 5: Performance comparison of **CORE** coarse and fine method on the **Multi-IHC CRC** Dataset in μm .

Resolution	Method	AArTRE [μm]	AMrTRE [μm]	AMxrTRE [μm]	Avg Time (s)
Coarse	Initial	0.18079	0.15209	0.36154	-
	DFBR [5]	0.0050	0.0031	0.0188	50.1357
	DeeperHistReg [4]	0.0049	0.0029	0.0196	70
	CORE	0.00431	0.0024	0.0153	14.37
Fine	CORE	0.002281	0.0011	0.0142	2172

Table 6: Performance comparison of **CORE** coarse and fine method on the **REACTIVAS** (H&E, PAS and mIF) dataset in μm .

Resolution	Technique	PAS Sections		mIF Sections	
		AMTRE [μm]	Avg Time(s)	AMTRE [μm]	Avg Time(s)
Coarse	DFBR [5]	2.89248	50	5.3920	50.135
	DeeperHistReg [35]	2.7072	70	3.6709	70
	CORE	1.0272	14.37	2.0495	14.37
Fine	CORE	0.36	1500	0.8460	1500

generalisable and reliable than traditional handcrafted or intensity-based approaches, particularly in complex multimodal scenarios.

Incorporation of nuclei-based point set registration further enhances alignment at the cellular level, a crucial aspect for downstream applications such as spatial transcriptomics, single-cell phenotyping, and microenvironment analysis. This local refinement ensures that biologically significant structures are accurately aligned, going beyond tissue-level correlation to enable precise cellular mapping.

The main reason we developed a machine learning-based nuclei detection approach, rather than a deep learning model, is that deep learning methods require extensive dataset-specific annotated nuclei data which most slides used for registration lack. To ensure generalisability across datasets, we therefore designed a classical machine learning-based nuclei detection pipeline.

Table A.10 summarises the processing time for each step in the CORE method on both the CPU and GPU platforms. Finally, we investigate the effect of regularisation on accurately preserving tissue morphology during deformation. We conducted extensive ablation studies to evaluate the robustness of our method and to understand the influence of key hyperparameters. Our approach outperforms existing methods in terms of the relative target registration error (rTRE), reinforcing the value of combining structural deep features with biological landmarks. This dual-level strategy is particularly beneficial in cases where modality-specific artefacts or variations, such as uneven staining, fixation-induced deformation, or differences in section thickness, can confound coarse-level methods.

However, there are limitations to consider; the fine registration stage depends on accurate nuclei detection, which can be hindered by overlapping cells, staining artefacts, or suboptimal segmentation in dense tissue regions. A key limitation of our approach is that the fine, shape-aware point-set registration stage is more time-consuming than coarse-level techniques. Nevertheless, this stage delivers substantial performance gains, achieving highly precise nuclei-level alignment for re-stained slides and fine tissue-level alignment for consecutive sections. The overall runtime could be further reduced by integrating faster deep learning models for nuclei detection, thereby enhancing computational efficiency, however it will require explicit training/finetuning for each dataset and we have not covered this aspect as part of the study. Moreover, while our feature extractor generalises well across modalities, performance may further improve with stain-specific fine-tuning or the integration of self-supervised domain adaptation techniques. Another consideration is the potential computational burden of full-resolution deformable registration, especially for high-resolution WSIs. Although our use of hierarchical processing

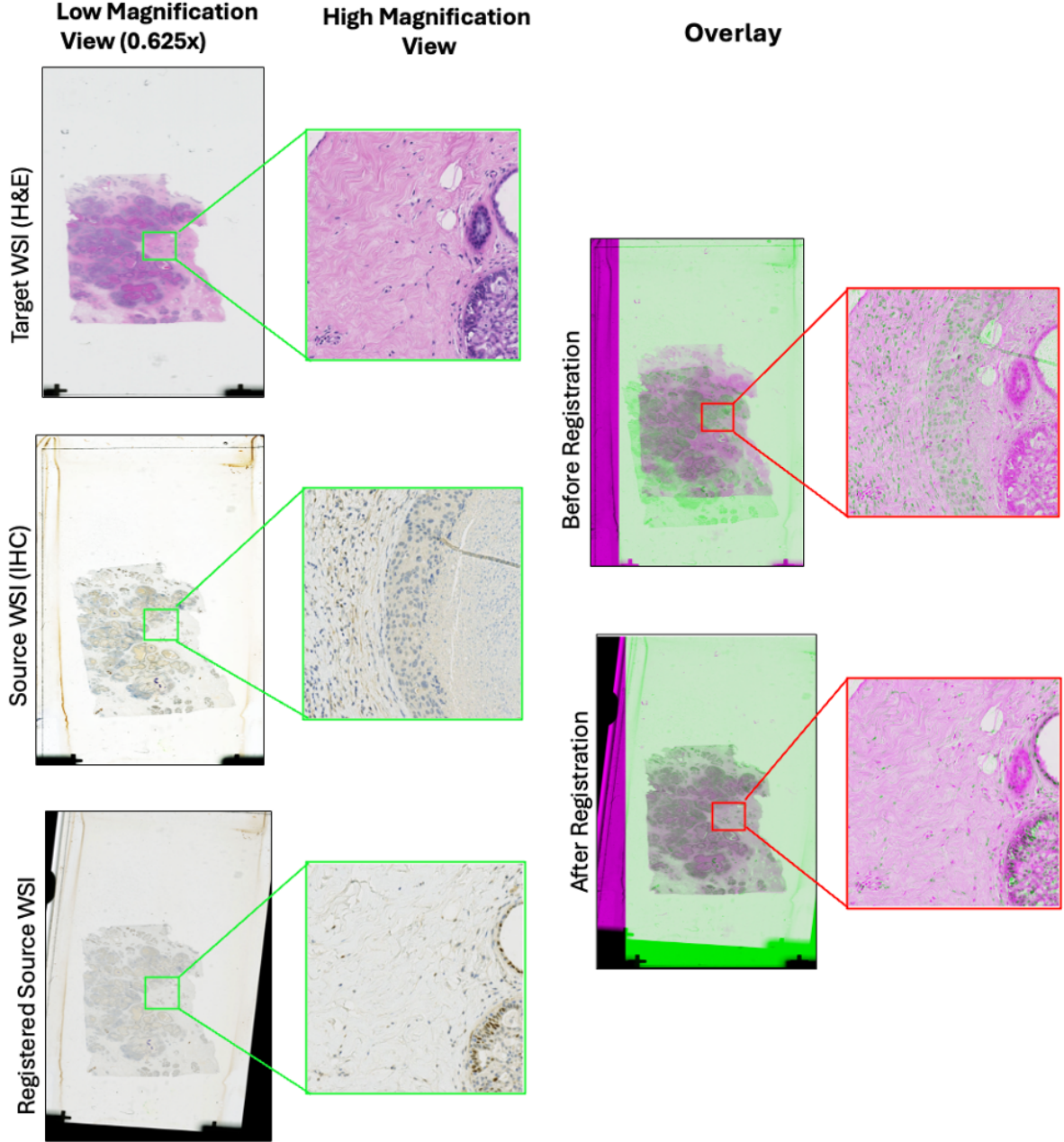


Figure 4: Multi-scale visualisation of CORE results on ACROBAT dataset. **Left column:** Low magnification views ($0.625\times$) of the target WSI (H&E), source WSI (IHC), and registered source WSI. **Middle column:** High magnification views of selected regions (indicated by green boxes) showing detailed tissue structures. **Right column:** Overlay comparison before and after registration, displayed at both low and high resolution (red boxes), demonstrating improved alignment of tissue structures following registration.

mitigates this to some extent, further acceleration, possibly via parallel optimisation, could enhance scalability.

In summary, this study demonstrates that combining deep feature-based global alignment with biologically informed local refinement is a powerful strategy for multimodal WSI registration. Our findings provide a foundation for the advancement of spatial

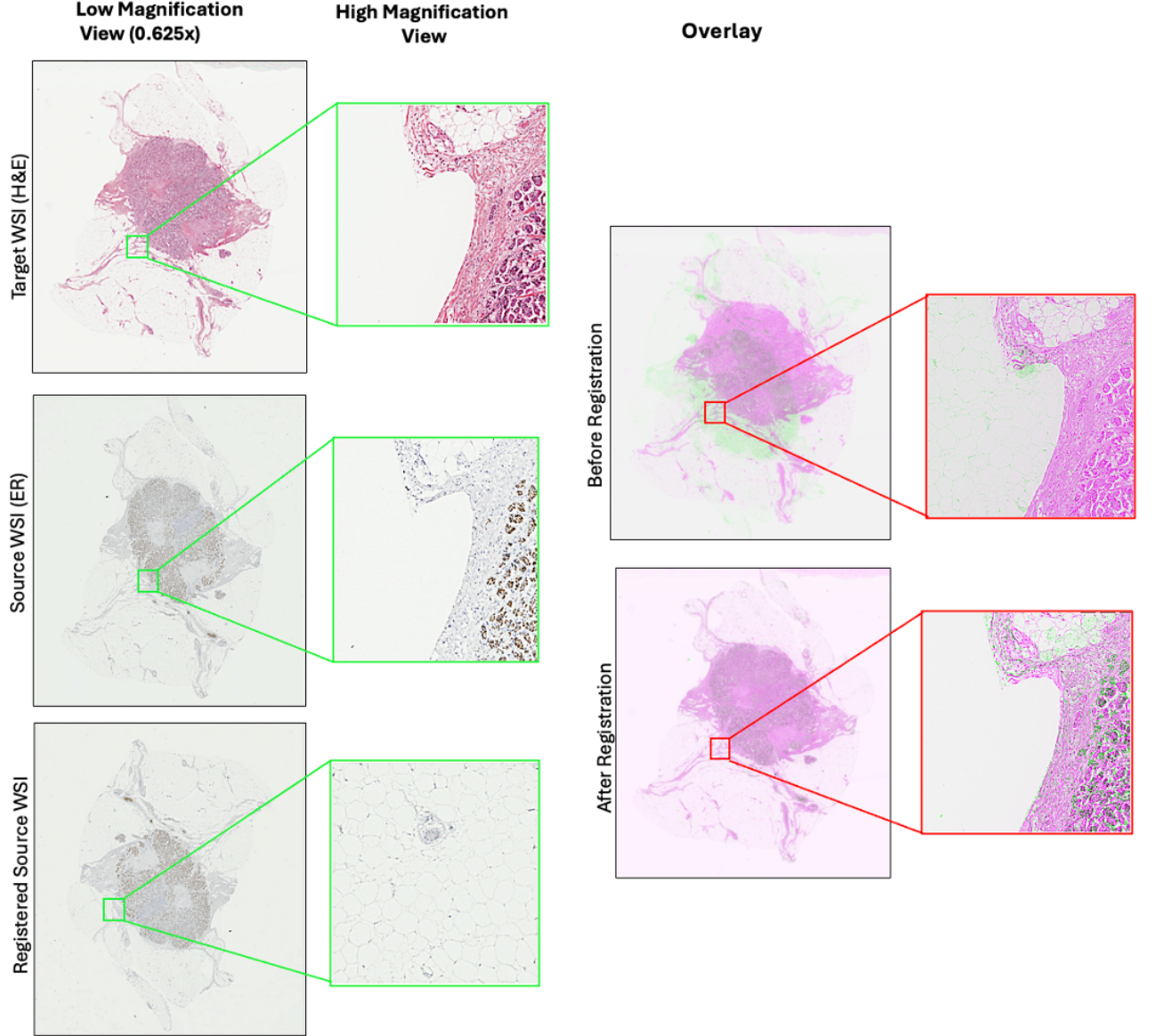


Figure 5: Multi-scale visualisation of CORE results on ANHIR dataset. **Left column:** Low magnification views ($0.625\times$) of the target WSI (H&E), source WSI (ER), and registered source WSI. **Middle column:** High magnification views of selected regions (indicated by green boxes) showing detailed tissue structures. **Right column:** Overlay comparison before and after registration, displayed at both low and high resolution (red boxes), demonstrating improved alignment of tissue structures following registration.

analysis in digital pathology and the integration of complex, multidimensional biological data.

5 Conclusions

We proposed a coarse-to-fine registration framework **CORE** for WSI alignment across diverse staining modalities, including H&E, IHC, PAS, and mIF. Our approach addresses

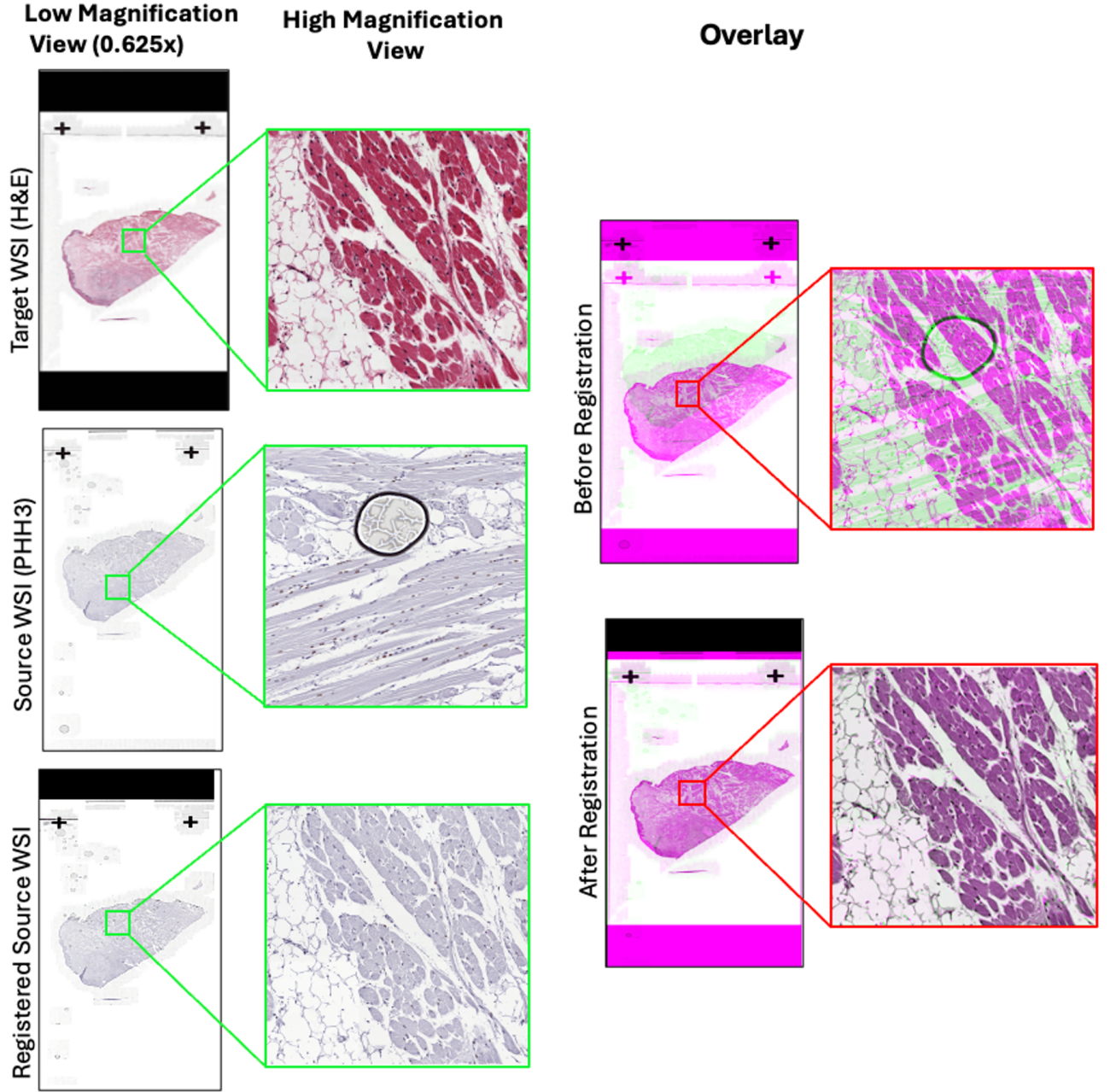


Figure 6: Multi-scale visualisation of CORE results on HYRECO dataset. **Left column:** Low magnification views ($0.625\times$) of the target WSI (H&E), source WSI (PAS), and registered source WSI. **Middle column:** High magnification views of selected regions (indicated by green boxes) showing detailed tissue structures. **Right column:** Overlay comparison before and after registration, displayed at both low and high resolution (red boxes), demonstrating improved alignment of tissue structures following registration.

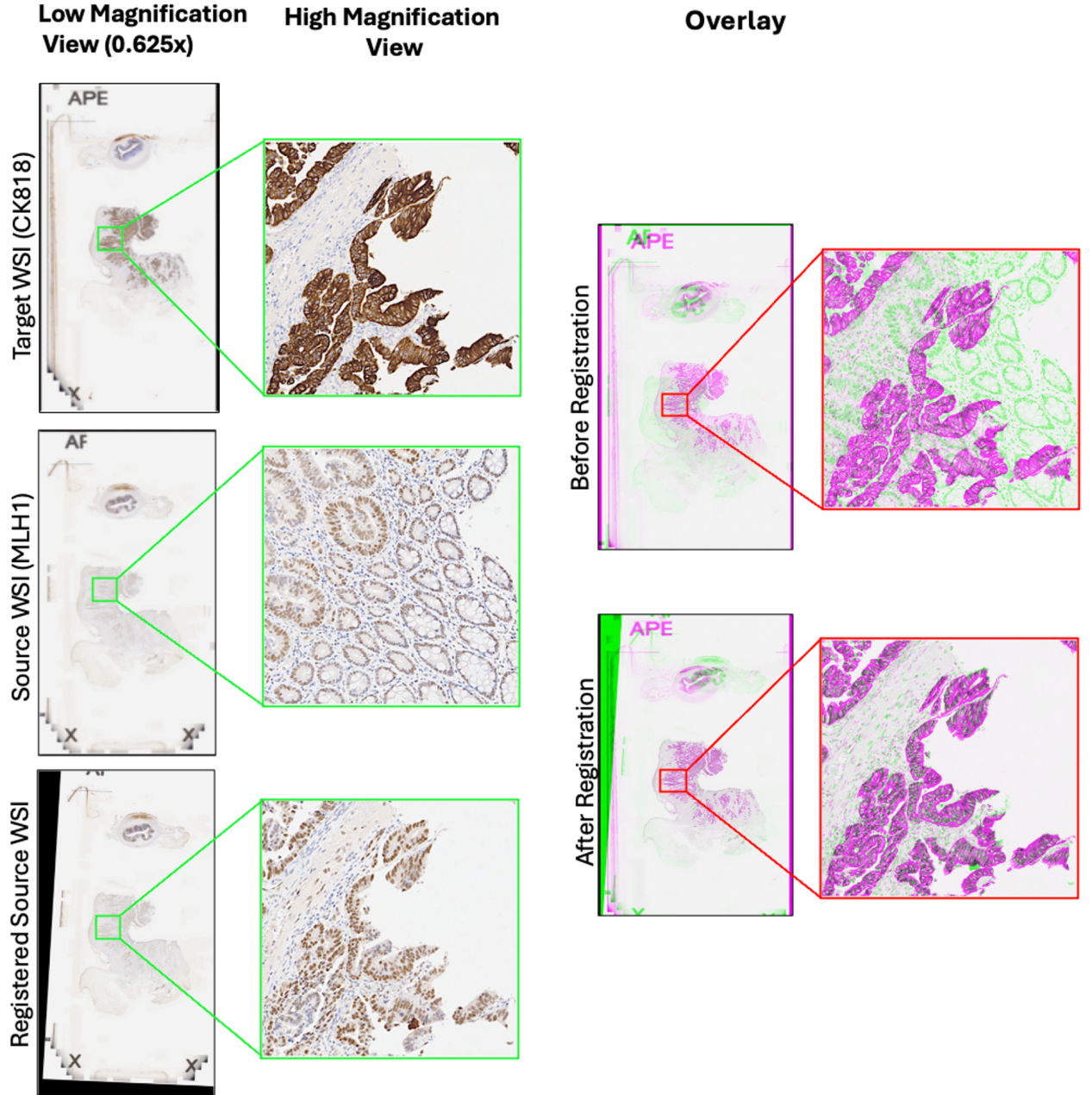


Figure 7: Multi-scale visualisation of CORE results on Multi-IHC CRC dataset. **Left column:** Low magnification views ($0.625\times$) of the target WSI (CK818), source WSI (MLH1), and registered source WSI. **Middle column:** High magnification views of selected regions (indicated by green boxes) showing detailed tissue structures. **Right column:** Overlay comparison before and after registration, displayed at both low and high resolution (red boxes), demonstrating improved alignment of tissue structures following registration.

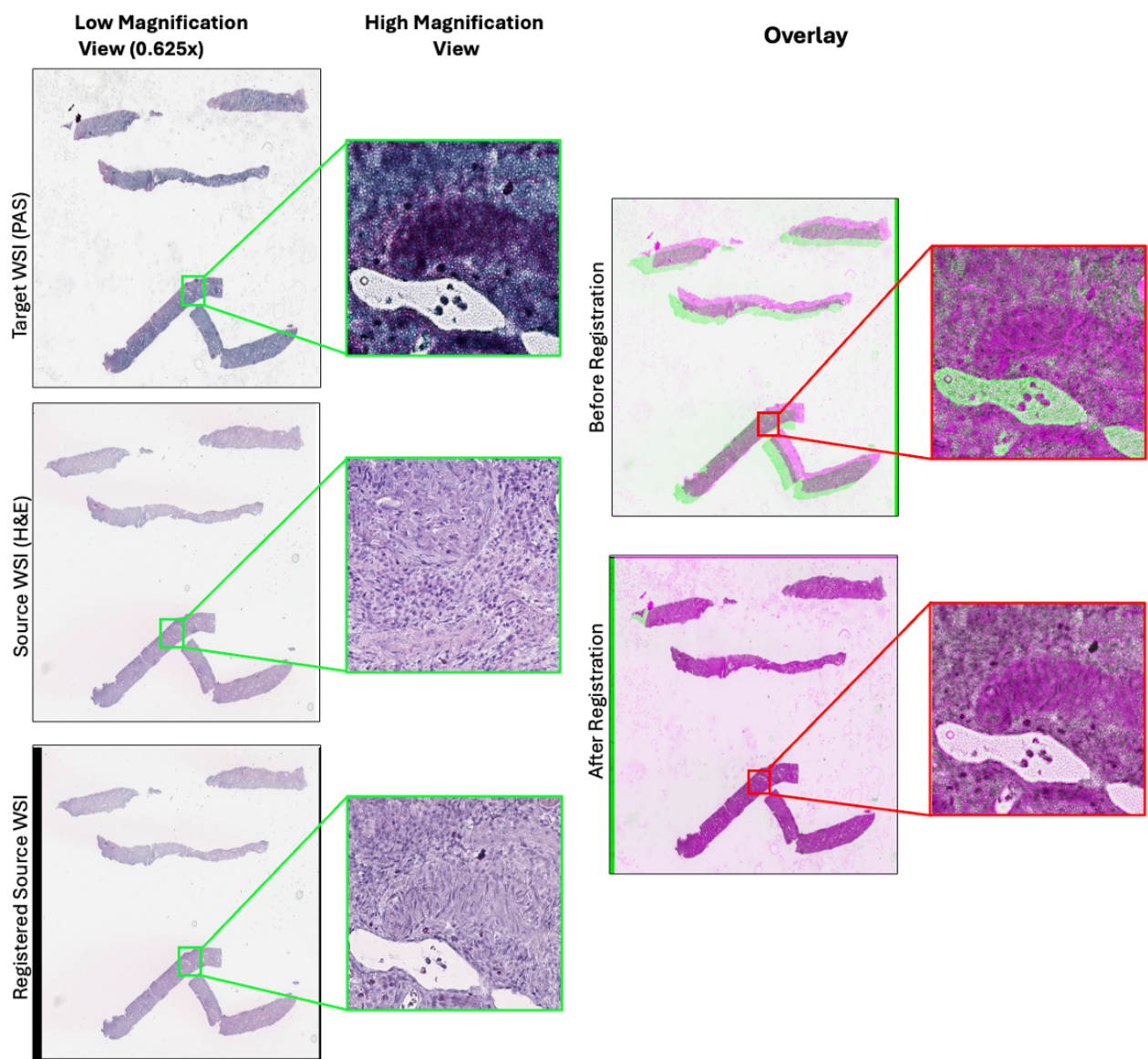


Figure 8: Multi-scale visualisation of CORE results on REACTIVAS dataset. **Left column:** Low magnification views ($0.625\times$) of the target WSI (PAS), source WSI (H&E), and registered source WSI. **Middle column:** High magnification views of selected regions (indicated by green boxes) showing detailed tissue structures. **Right column:** Overlay comparison before and after registration, displayed at both low and high resolution (red boxes) levels, demonstrating improved alignment of tissue structures following registration.

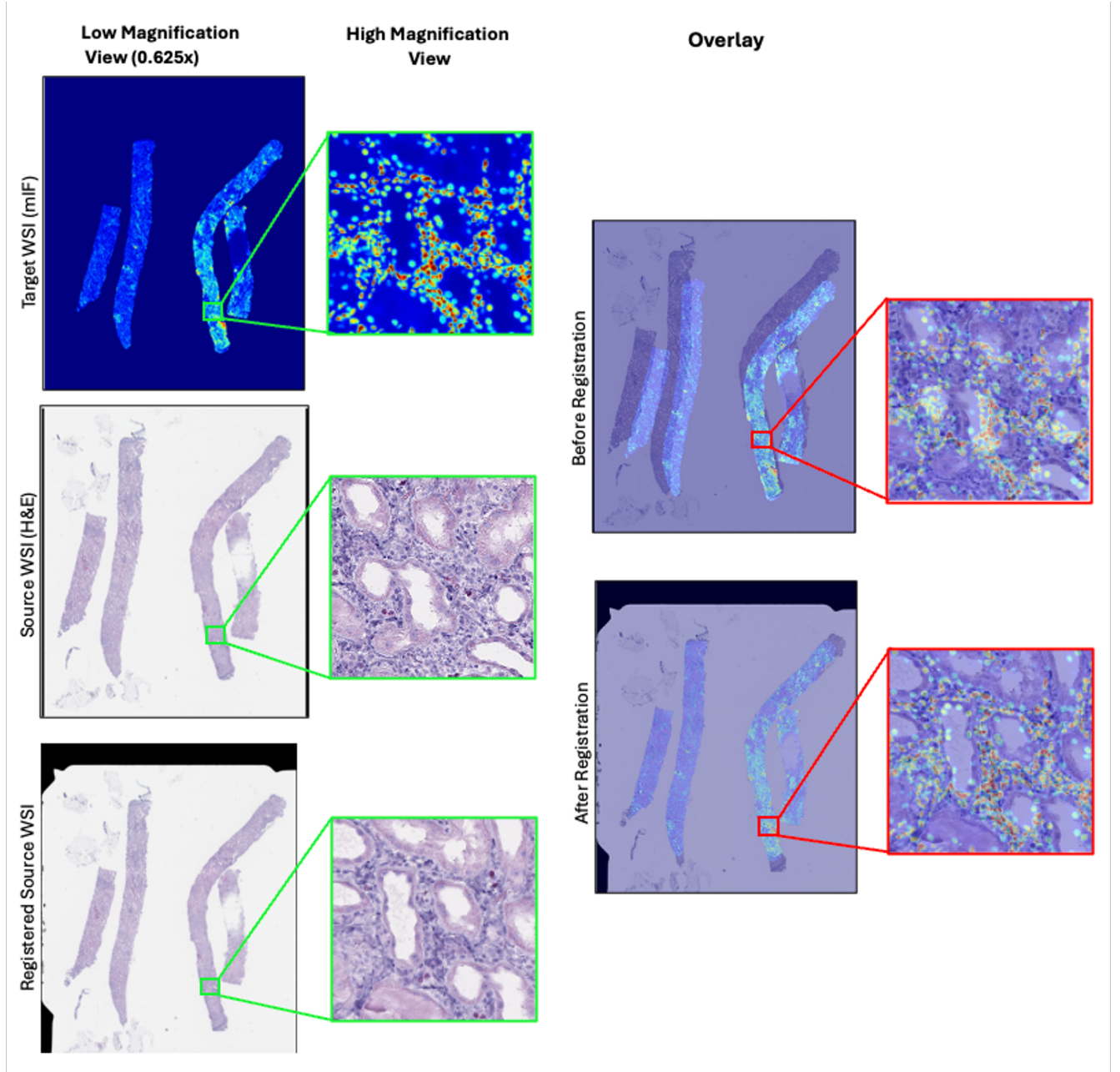


Figure 9: Multi-scale visualisation of CORE results on REACTIVAS dataset. **Left column:** Low magnification views ($0.625\times$) of the target WSI (mIF), source WSI (H&E), and registered source WSI. **Middle column:** High magnification views of selected regions (indicated by green boxes) showing detailed tissue structures. **Right column:** Overlay comparison before and after registration, displayed at both low and high resolution (red boxes), demonstrating improved alignment of tissue structures following registration.

the complex challenges of multimodal alignment by combining efficient pre-processing, robust feature extraction, and biologically informed refinement.

The pipeline begins with tissue mask extraction using Florence-2-SAM for prompt-based segmentation, allowing precise isolation of tissue regions. This is followed by an initial rigid alignment based on geometric transformation of the tissue mask centroids.

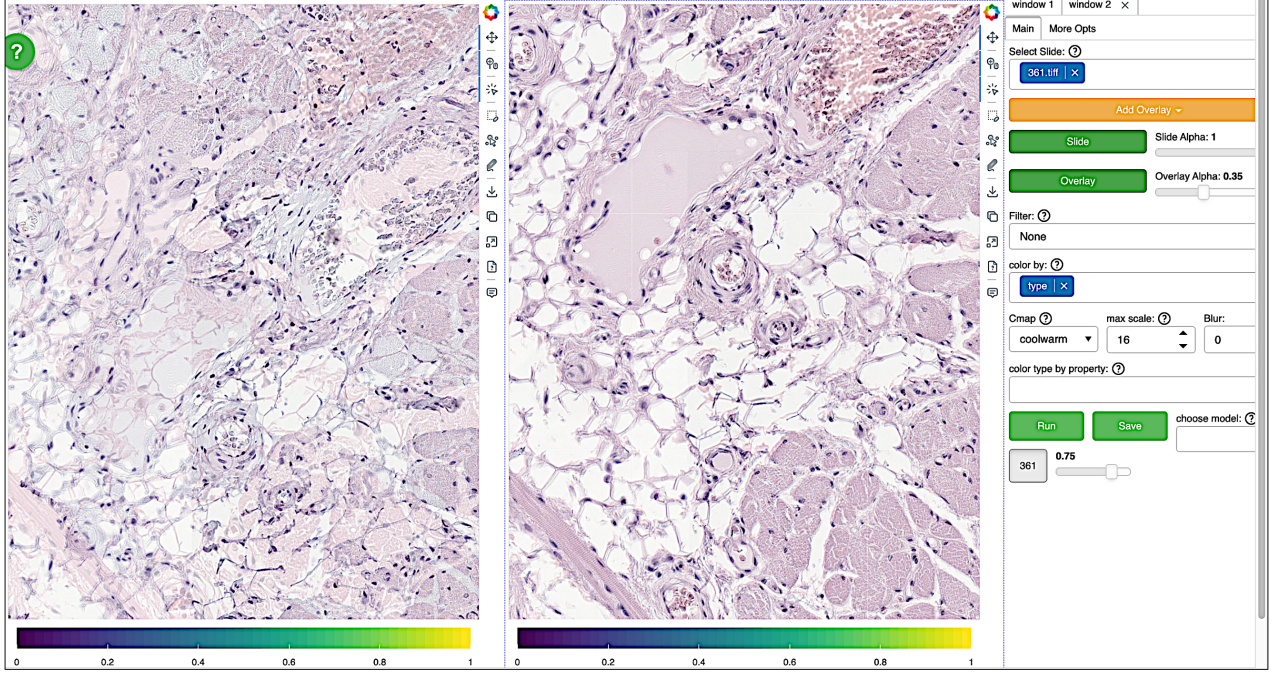


Figure 10: TiaViz Visualisation tool displaying source(PHH3) and target(H&E) re-stained slides before and after registration. **(Left)** Target overlaid on source before alignment. **(Right)** Target overlaid on source after alignment.

We then apply XFeat for fast and dense deep feature extraction to refine the alignment and iteratively optimise a coarse deformation field using adaptive regularisation.

In the fine registration stage, nuclei are detected in both target and coarsely registered source slides. The shape-aware point set registration is performed at full resolution, followed by deformable alignment using the CPD algorithm to achieve cellular-level precision.

Evaluation on multiple datasets demonstrate that our approach achieves high registration accuracy with strong computational efficiency, outperforming existing methods across multiple datasets. This framework lays a robust foundation for multimodal histopathological analysis, allowing accurate cross-modality correlation and paving the way for more effective computer-aided diagnostic systems.

Acknowledgements

SEAR and BE report financial support by the MRC (MR/X011585/1). SEAR and NR are grateful to the European Commission, which provided funding through the Innovative Medicines Initiative 2 Joint Undertaking under grant agreement No 945358. AS and SEAR received financial support from the British Council (project ref: 1203764217). The REACTIVAS study was partly supported from an Investigator-Initiated Program of Merck Sharp & Dohme Corp (MSD). The opinions expressed are those of the authors and do not necessarily represent those of MSD. NR is CEO and CSO of Histofy Ltd.

References

- [1] Behnaz Elhaminia, Abdullah Alsalemi, Esha Nasir, Mostafa Jahanifar, Ruqayya Awan, Lawrence S. Young, Nasir M. Rajpoot, Fayyaz Minhas, and Shan E Ahmed Raza. From Traditional to Deep Learning Approaches in Whole Slide Image Registration: A Methodological Review, 2025. Version Number: 1.
- [2] Johannes Lotz, Nick Weiss, Jeroen van der Laak, and Stefan Heldmann. Comparison of Consecutive and Re-stained Sections for Image Registration in Histopathology. *Journal of Medical Imaging*, 10(06), November 2023. arXiv:2106.13150 [eess].
- [3] Chandler D. Gatenbee, Ann-Marie Baker, Sandhya Prabhakaran, Otilie Swinyard, Robbert J. C. Slebos, Gunjan Mandal, Eoghan Mulholland, Noemi Andor, Andriy Marusyk, Simon Leedham, Jose R. Conejo-Garcia, Christine H. Chung, Mark Robertson-Tessi, Trevor A. Graham, and Alexander R. A. Anderson. Virtual alignment of pathology image series for multi-gigapixel whole slide images. *Nature Communications*, 14(1):4502, July 2023.
- [4] Marek Wodzinski, Niccolò Marini, Manfredo Atzori, and Henning Müller. Deeper-HistReg: Robust Whole Slide Images Registration Framework, 2024. Version Number: 1.
- [5] Ruqayya Awan, Shan E. Ahmed Raza, Johannes Lotz, Nick Weiss, and Nasir Rajpoot. Deep feature based cross-slide registration. *Computerized Medical Imaging and Graphics*, 104:102162, March 2023.
- [6] J. Lotz, J. Olesch, B. Muller, T. Polzin, P. Galuschka, J. M. Lotz, S. Heldmann, H. Laue, M. Gonzalez-Vallinas, A. Warth, B. Lahrmann, N. Grabe, O. Sedlaczek, K. Breuhahn, and J. Modersitzki. Patch-Based Nonlinear Image Registration for Gigapixel Whole Slide Images. *IEEE Transactions on Biomedical Engineering*, 63(9):1812–1819, September 2016.
- [7] Johannes Lotz, Nick Weiss, and Stefan Heldmann. Robust, fast and accurate: a 3-step method for automatic histological image registration, 2019. Version Number: 2.
- [8] Jiri Borovec, Jan Kybic, Ignacio Arganda-Carreras, Dmitry V. Sorokin, Gloria Bueno, Alexander V. Khvostikov, Spyridon Bakas, Eric I-Chao Chang, Stefan Heldmann, Kimmo Kartasalo, Leena Latonen, Johannes Lotz, Michelle Noga, Sarthak Pati, Kumaradevan Punithakumar, Pekka Ruusuvuori, Andrzej Skalski, Nazanin Tahmasebi, Masi Valkonen, Ludovic Venet, Yizhe Wang, Nick Weiss, Marek Wodzinski, Yu Xiang, Yan Xu, Yan Yan, Paul Yushkevich, Shengyu Zhao, and Arrate Munoz-Barrutia. ANHIR: Automatic Non-Rigid Histological Image Registration Challenge. *IEEE Transactions on Medical Imaging*, 39(10):3042–3052, October 2020.
- [9] Philippe Weitz, Masi Valkonen, Leslie Solorzano, Circe Carr, Kimmo Kartasalo, Constance Boissin, Sonja Koivukoski, Aino Kuusela, Dusan Rasic, Yanbo Feng, Sandra Sinius Pouplier, Abhinav Sharma, Kajsa Ledesma Eriksson, Stephanie Robertson, Christian Marzahl, Chandler D. Gatenbee, Alexander R.A. Anderson, Marek Wodzinski, Artur Jurgas, Niccolò Marini, Manfredo Atzori, Henning Müller, Daniel Budelmann, Nick Weiss, Stefan Heldmann, Johannes Lotz, Jelmer M. Wolterink,

- Bruno De Santi, Abhijeet Patil, Amit Sethi, Satoshi Kondo, Satoshi Kasai, Kousuke Hirasawa, Mahtab Farrokh, Neeraj Kumar, Russell Greiner, Leena Latonen, Anne-Vibeke Laenkholm, Johan Hartman, Pekka Ruusuvuori, and Mattias Rantalainen. The ACROBAT 2022 challenge: Automatic registration of breast cancer tissue. *Medical Image Analysis*, 97:103257, October 2024.
- [10] Stefan Leutenegger, Margarita Chli, and Roland Y. Siegwart. BRISK: Binary Robust invariant scalable keypoints. In *2011 International Conference on Computer Vision*, pages 2548–2555, Barcelona, Spain, November 2011. IEEE.
 - [11] Anindya Sarkar, Quan Yuan, and Chukka Srinivas. A robust method for inter-marker whole slide registration of digital pathology images using lines based features. In *2014 IEEE 11th International Symposium on Biomedical Imaging (ISBI)*, pages 762–765, Beijing, April 2014. IEEE.
 - [12] Martin A. Fischler and Robert C. Bolles. Random sample consensus: a paradigm for model fitting with applications to image analysis and automated cartography. *Communications of the ACM*, 24(6):381–395, June 1981.
 - [13] Xingyue Wei, Lin Ge, Lijie Huang, Jianwen Luo, and Yan Xu. Unsupervised Non-Rigid Histological Image Registration Guided by Keypoint Correspondences Based on Learnable Deep Features With Iterative Training. *IEEE Transactions on Medical Imaging*, 44(1):447–461, January 2025.
 - [14] Vladislav A. Pyatov and Dmitry V. Sorokin. Unsupervised Feature Matching for Affine Histological Image Registration. In Apostolos Antonacopoulos, Subhasis Chaudhuri, Rama Chellappa, Cheng-Lin Liu, Saumik Bhattacharya, and Uma-pada Pal, editors, *Pattern Recognition*, volume 15313, pages 34–48. Springer Nature Switzerland, Cham, 2025. Series Title: Lecture Notes in Computer Science.
 - [15] Lin Ge, Xingyue Wei, Yayu Hao, Jianwen Luo, and Yan Xu. Unsupervised Histological Image Registration Using Structural Feature Guided Convolutional Neural Network. *IEEE Transactions on Medical Imaging*, 41(9):2414–2431, September 2022. Publisher: Institute of Electrical and Electronics Engineers (IEEE).
 - [16] Paul-Edouard Sarlin, Daniel DeTone, Tomasz Malisiewicz, and Andrew Rabinovich. SuperGlue: Learning Feature Matching With Graph Neural Networks. In *2020 IEEE/CVF Conference on Computer Vision and Pattern Recognition (CVPR)*, pages 4937–4946, Seattle, WA, USA, June 2020. IEEE.
 - [17] Awan R and Rajpoot N. Deep autoencoder features for registration of histology images. In *Annual Conference on Medical Image Understanding and Analysis*, pages 371–378. Springer, 2018.
 - [18] Dosovitskiy A, Fischer P, Ilg E, Hausser P, Hazirbas C, Golkov V, Van Der Smagt P, Cremers D, and Brox T. FlowNet: Learning optical flow with convolutional networks. In *Proceedings of the IEEE international conference on computer vision*, pages 2758–2766, 2015.
 - [19] Dwarikanath Mahapatra. Registration of Histopathology Images Using Structural Information From Fine Grained Feature Maps, 2020. Version Number: 1.

- [20] Adith Jeyasangar, Abdullah Alsalemi, and Shan E. Ahmed Raza. Nuclei-Location Based Point Set Registration of Multi-stained Whole Slide Images. In Moi Hoon Yap, Connah Kendrick, Ardhendu Behera, Timothy Cootes, and Reyer Zwiggelaar, editors, *Medical Image Understanding and Analysis*, volume 14859, pages 372–386. Springer Nature Switzerland, Cham, 2024. Series Title: Lecture Notes in Computer Science.
- [21] Jeroen van der Laak, Johannes Lotz, Nick Weiss, and Stefan Heldmann. HyReCo - Hybrid re-stained and consecutive histological serial sections, July 2021.
- [22] Jun Jiang, Raymond Moore, Brenna Novotny, Leo Liu, Zachary Fogarty, Ray Guo, Markovic Svetomir, and Chen Wang. Multimodal Alignment of Histopathological Images Using Cell Segmentation and Point Set Matching for Integrative Cancer Analysis, 2024. Version Number: 1.
- [23] Chandler Gatenbee. Source data for VALIS: Virtual Alignment of pathoLOGY Image Series for multi-gigapixel whole slide images publication, May 2023.
- [24] Joshua Doyle, Benjamin F. Green, Margaret Eminizer, Daniel Jimenez-Sanchez, Steve Lu, Elizabeth L. Engle, Haiying Xu, Aleksandra Ogurtsova, Jonathan Lai, Sigfredo Soto-Diaz, Jeffrey S. Roskes, Julie S. Deutsch, Janis M. Taube, Joel C. Sunshine, and Alexander S. Szalay. Whole-Slide Imaging, Mutual Information Registration for Multiplex Immunohistochemistry and Immunofluorescence. *Laboratory Investigation*, 103(8):100175, August 2023.
- [25] Marc Macenko, Marc Niethammer, J. S. Marron, David Borland, John T. Woosley, Xiaojun Guan, Charles Schmitt, and Nancy E. Thomas. A method for normalizing histology slides for quantitative analysis. In *2009 IEEE International Symposium on Biomedical Imaging: From Nano to Macro*, pages 1107–1110, Boston, MA, USA, June 2009. IEEE.
- [26] Bin Xiao, Haiping Wu, Weijian Xu, Xiyang Dai, Houdong Hu, Yumao Lu, Michael Zeng, Ce Liu, and Lu Yuan. Florence-2: Advancing a Unified Representation for a Variety of Vision Tasks, 2023. Version Number: 1.
- [27] Alexander Kirillov, Eric Mintun, Nikhila Ravi, Hanzi Mao, Chloe Rolland, Laura Gustafson, Tete Xiao, Spencer Whitehead, Alexander C. Berg, Wan-Yen Lo, Piotr Dollár, and Ross Girshick. Segment Anything, April 2023. arXiv:2304.02643 [cs].
- [28] Guilherme Potje, Felipe Cadar, Andre Araujo, Renato Martins, and Erickson R. Nascimento. XFeat: Accelerated Features for Lightweight Image Matching, 2024. Version Number: 1.
- [29] Brian B. Avants, Nicholas J. Tustison, Gang Song, Philip A. Cook, Arno Klein, and James C. Gee. A reproducible evaluation of ANTs similarity metric performance in brain image registration. *NeuroImage*, 54(3):2033–2044, February 2011. Publisher: Elsevier BV.
- [30] Guha Balakrishnan, Amy Zhao, Mert R. Sabuncu, John Guttag, and Adrian V. Dalca. VoxelMorph: A Learning Framework for Deformable Medical Image Registration. 2018. Publisher: arXiv Version Number: 3.

- [31] Dan Ruan, Jeffrey A. Fessler, Michael Roberson, James Balter, and Marc Kessler. Nonrigid registration using regularization that accomodates local tissue rigidity. In Joseph M. Reinhardt and Josien P. W. Pluim, editors, *SPIE Proceedings*, volume 6144, page 614412, San Diego, CA, March 2006. SPIE. ISSN: 0277-786X.
- [32] Andriy Myronenko and Xubo Song. Point Set Registration: Coherent Point Drift. *IEEE Transactions on Pattern Analysis and Machine Intelligence*, 32(12):2262–2275, December 2010. Publisher: Institute of Electrical and Electronics Engineers (IEEE).
- [33] ClinicalTrials.gov. Study details: Nct04916704 — subclinical cytomegalovirus reactivation in acute anca-associated vasculitis. <https://clinicaltrials.gov/study/NCT04916704>, 2024. Accessed: 2024-01-01.
- [34] Marek Wodzinski and Andrzej Skalski. Multistep, automatic and nonrigid image registration method for histology samples acquired using multiple stains. *Physics in Medicine & Biology*, November 2020.
- [35] Marek Wodzinski, Niccolò Marini, Manfredo Atzori, and Henning Müller. RegWSI: Whole slide image registration using combined deep feature- and intensity-based methods: Winner of the ACROBAT 2023 challenge. *Computer Methods and Programs in Biomedicine*, 250:108187, June 2024.
- [36] Johnathan Pocock, Simon Graham, Quoc Dang Vu, Mostafa Jahanifar, Srijay Deshpande, Giorgos Hadjigeorgiou, Adam Shephard, Raja Muhammad Saad Bashir, Mohsin Bilal, Wenqi Lu, David Epstein, Fayyaz Minhas, Nasir M. Rajpoot, and Shan E Ahmed Raza. TIAToolbox as an end-to-end library for advanced tissue image analytics. *Communications Medicine*, 2(1):120, September 2022.

A Supplementary Details

Fig. A.1 shows comparison of tissue staining techniques: (Left) Haematoxylin staining highlights cell nuclei in blue. (Middle) Immunohistochemistry using an antibody-chromogen system detects a specific protein in brown. (Right) Multiplex immunofluorescence allows simultaneous visualisation of multiple markers, with nuclei staining with DAPI coloured in blue and other markers in green and red.

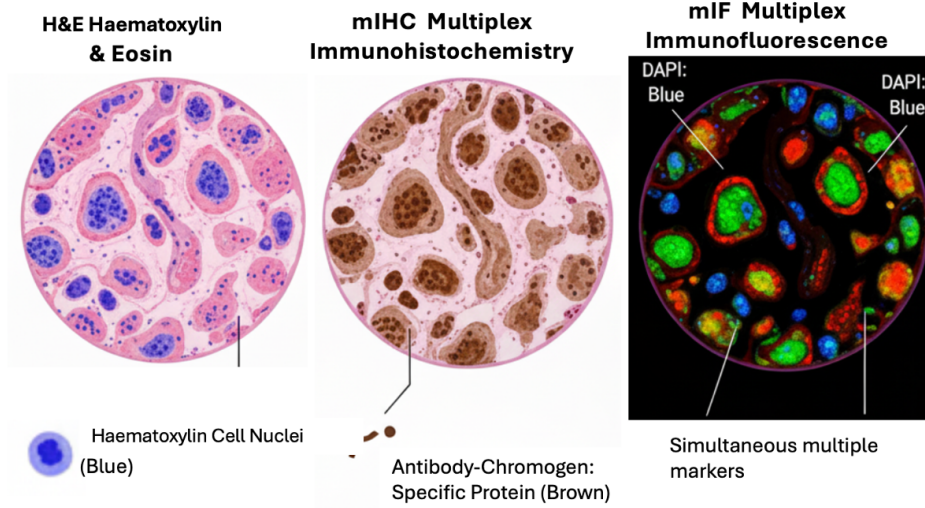


Figure A.1: (Left to Right) Staining Types (1) H&E (2) mIHC (3) mIF.

Using the demo: To facilitate real-time deformation of the source image and simultaneous visualisation of the transformed and target WSIs, we provide a dedicated viewer, *TIAViz*. The tool is available as part of the *TIAToolbox* library [36], which can be installed via `pip`. The demo can be used by following the steps below:

1. **Install TIAViz.** Install the *TIAToolbox* package using `pip`.
2. **Prepare the directory structure.** Within the working directory, create two subdirectories named `slides` and `overlays`.
3. **Place the required files.** Store the source WSI in the `slides` directory. Store the target WSI together with deformation field in the `overlays` directory.
4. **Ensure filename consistency.** All corresponding files must share the same stem name so that *TIAViz* can automatically match the source, target, and deformation field.
5. **Launch the viewer.** Start the *TIAViz* interface using the `tiavisualize` command, either from the command line or within a Python notebook, specifying the paths to the `slides` and `overlays` directories.
6. **Registration visualisation.** From the `slides` dropdown in the top-left panel, first select the source slide. After this, choose the deformation field from the `overlay` dropdown; the deformation will be applied to the source slide within a

few seconds. Next, select the target slide from the **Overlay** dropdown to display it on top of the registered source. Use the right-hand panel to adjust the alpha values of both layers to achieve optimal visualisation of the alignment.

Stain Normalisation: Stain Normalisation is often required for H&E slides because their colour appearance varies widely across laboratories, scanners, and staining batches, which can affect how prompt-based models such as Florence-SAM [26] detect tissue boundaries. Normalising H&E reduces this variability and provides a more consistent input for tissue mask extraction. In contrast, IHC slides uses stable chromogens such as DAB that have less colour variability, and convey biologically meaningful intensity differences that normalisation could distort, so stain normalisation is generally unnecessary for IHC.

Table A.1: Definitions of relative Target Registration Error (rTRE) metrics used in evaluation.

Abbreviation Definition	
AArTRE	Average Absolute relative Target Registration Error
AMrTRE	Average Median relative Target Registration Error
MArTRE	Median Absolute relative Target Registration Error
MMrTRE	Median Median relative Target Registration Error
AMxrTRE	Average Maximum relative Target Registration Error
AMrTRE	Average Mean relative Target Registration Error

Table A.2: Coarse level deformation estimation parameters.

Parameter	Value
Similarity Metric	NCC
Optimiser	Adam
Regulariser	Adaptive
Interpolation Method	Bilinear
Learning Rate	0.001
Iterations	200~500

Table A.3: Shape-aware nuclei based registration parameters.

Parameter	Symbol	Description	Default	Range
Shape Weight	γ	Spatial vs. shape trade-off	0.3	[0.0, 1.0]
Tolerance	ε	optimisation convergence threshold	10^{-8}	$[10^{-8}, 10^{-4}]$
Max Iterations	i_{\max}	Maximum number of optimisation steps	100	[50, 500]
Reg. Strength	λ	Weight of regularisation penalty	1.0	[0.1, 10.0]
Smoothness	β	Controls smoothness of deformation field	2.0	[1.0, 5.0]
k-d Leaf Size	k	Leaf size for nearest-neighbour queries	10	[5, 50]

Table A.4: Non-Rigid registration parameters.

Parameter	Symbol	Default	Range	Description
Regularisation Weight	α	0.01	[0.001, 0.1]	Controls smoothness vs. data fidelity
Smoothness Parameter	β	0.5	[0.1, 2.0]	Gaussian kernel bandwidth
Maximum Iterations	i_{\max}	200	[100, 500]	EM algorithm iteration limit
Convergence Tolerance	ε	1×10^{-9}	$[1 \times 10^{-12}, 1 \times 10^{-6}]$	Weight change threshold
Outlier Weight	w	0.1	[0.01, 0.3]	Uniform distribution weight
Initial Variance	σ_{init}^2	1.0	[0.1, 5.0]	Initial Gaussian variance
Gaussian Smoothing	σ	10.0	[5.0, 20.0]	Dense field smoothing
Max Displacement	d_{\max}	10.0	[5.0, 50.0]	Maximum pixel displacement

Table A.5: Performance comparison of **CORE** rigid registration method on the **HYRECO** Dataset (Consecutive and Re-stained tissue sections).

Type	Resolution Technique	Consecutive Sections			Re-stained Sections	
		AMTRE [μm]	AATRE [μm]	Avg Time (s)	AMTRE [μm]	Avg Time (s)
Rigid	Coarse	DFBR [5]	542.42	1754.52	240	30.03
		AGH [34]	442.73	753.13	150	28.58
		DeeperHistReg [35]	174.9	234.5	120	12.24
		HistokatFusion [2]	20.12	62.58	50.13	2.00
		CORE	65.26	109.83	18	6.81
	Fine	CORE	39.20	60.21	2340	2.26

Table A.6: Stepwise results on the **ANHIR** dataset using average aggregation. Each alignment step progressively reduces error Median aggregation results.

Step	AArTRE	AMrTRE	AMxrTRE
Initial	0.1340	0.0665	0.2338
Coarse Transform	0.0040	0.0015	0.0240
Fine Transform	0.0034	0.0012	0.0323

Table A.7: Stepwise results on the **HYRECO** consecutive tissue sections using average aggregation. Each alignment step progressively reduces error Median aggregation results.

Step	AATRE	AMTRE	AMxTRE
Initial	3082.35	2583.96	7519.2
Coarse Transform	105.3	65.5	253.1
Fine Transform	5.02	4.35	2.83

Table A.8: Stepwise results on the **Multi-IHC CRC** using average aggregation. Each alignment step progressively reduces error Median aggregation results.

Step	AArTRE	AMrTRE	AMxrTRE
Initial	0.18079	0.15209	0.36154
Coarse Transform	0.00431	0.0024	0.0153
Fine Transform	0.002281	0.0011	0.0142

Table A.9: Stepwise results on the **REACTIVAS** using average aggregation. Each alignment step progressively reduces error Median aggregation results.

Step	AATRE	AMTRE	AMxTRE
Initial	209.098	150.43	400.51
Coarse Transform	1.57	1.0272	5.76
Fine Transform	0.45	0.36	1.24

Table A.10: Processing Time per Step (CPU vs GPU)

Step	Average CPU (sec)	Time GPU (sec)
Initial	0.29	0.50
Downsampling	0.80	0.67
Preprocessing	0.19	0.00
Tissue Mask Extraction	6.08	5.40
TriMorph	1.22	0.56
Evaluation	0.70	0.29
XFeat	2.91	0.80
Similarity Estimation	0.73	0.29
Warping	<0.01	0.00
Fine Point-set Rigid	456	299
Fine Point-set Non-Rigid	400	400